Forecasting the Observable Rates of Gravitationally Lensed Supernovae for the PASSAGES Dusty Starbursts

Downloaded from: https://research.chalmers.se, 2026-05-01 06:07 UTC

Citation for the original published paper (version of record):
Kamieneski, P., Windhorst, R., Frye, B. et al (2026). Forecasting the Observable Rates of Gravitationally Lensed Supernovae for the PASSAGES Dusty Starbursts. Astrophysical Journal, 1000(2). http://dx.doi.org/10.3847/1538-4357/ae459e

N.B. When citing this work, cite the original published paper.

research.chalmers.se offers the possibility of retrieving research publications produced at Chalmers University of Technology. It covers all kind of research output: articles, dissertations, conference papers, reports etc. since 2004. research.chalmers.se is administrated and maintained by Chalmers Library

(article starts on next page)

The Astrophysical Journal, 1000:235 (20pp), 2026 April 1 https://doi.org/10.3847/1538-4357/ae459e
© 2026. The Author(s). Published by the American Astronomical Society.
OPEN ACCESS

Forecasting the Observable Rates of Gravitationally Lensed Supernovae for the PASSAGES Dusty Starbursts

Patrick S. Kamieneski[1,2], Rogier A. Windhorst[1], Brenda L. Frye[3], Min S. Yun[4], Kevin C. Harrington[5,6,7], Simon D. Mork[1], Nicholas Foo[1], Nikhil Garuda[3], Massimo Pascale[8], Belén Alcalde Pampliega[5,9], Timothy Carleton[1], Seth H. Cohen[1], Carlos Garcia Diaz[4], Rolf A. Jansen[1], Eric F. Jiménez-Andrade[10], Anton M. Koekemoer[11], James D. Lowenthal[12], Allison Noble[1], Justin D. R. Pierel[11], Amit Vishwas[13], Q. Daniel Wang[4], and Ilsang Yoon[14]

[1] School of Earth and Space Exploration, Arizona State University, PO Box 876004, Tempe, AZ 85287-6004, USA; patrick.kamieneski@chalmers.se
[2] Department of Space, Earth and Environment, Chalmers University of Technology, SE-412 96 Gothenburg, Sweden
[3] Department of Astronomy/Steward Observatory, University of Arizona, 933 North Cherry Avenue, Tucson, AZ 85721-0009, USA
[4] Department of Astronomy, University of Massachusetts, Amherst, MA 01003, USA
[5] European Southern Observatory, Alonso de Córdova 3107, Vitacura, Casilla 19001, Santiago de Chile, Chile
[6] Joint ALMA Observatory, Alonso de Córdova 3107, Vitacura, Casilla 19001, Santiago de Chile, Chile
[7] National Astronomical Observatory of Japan, Los Abedules 3085 Oficina 701, Vitacura 763 0414, Santiago, Chile
[8] Department of Astronomy, University of California, 501 Campbell Hall #3411, Berkeley, CA 94720, USA
[9] SKA Observatory, Jodrell Bank, SK11 9FT, UK
[10] Instituto de Radioastronomía y Astrofísica, Universidad Nacional Autónoma de México, Antigua Carretera a Pátzcuaro # 8701, Ex-Hacienda San José de la Huerta, Morelia, Michoacán, C.P. 58089, Mexico
[11] Space Telescope Science Institute, 3700 San Martin Drive, Baltimore, MD 21218, USA
[12] Smith College, Northampton, MA 01063, USA
[13] Cornell Center for Astrophysics and Planetary Science, Cornell University, Space Sciences Building, Ithaca, NY 14853, USA
[14] National Radio Astronomy Observatory, 520 Edgemont Road, Charlottesville, VA 22903, USA
Received 2025 August 14; revised 2026 February 6; accepted 2026 February 11; published 2026 March 26

Abstract

More than 60 years have passed since the first formal suggestion to use strongly lensed supernovae (SNe) to measure the expansion rate of the Universe through time-delay cosmography. Yet, fewer than 10 such objects have ever been discovered. We consider the merits of a targeted strategy focused on lensed hyperluminous infrared galaxies, which are among the most rapidly star-forming galaxies known in the Universe. With star formation rates (SFRs) $\sim$200–6000 $M_{\odot}\,\mathrm{yr}^{-1}$, the $\sim$30 objects in the Planck All-Sky Survey to Analyze Gravitationally-lensed Extreme Starbursts are excellent candidates for a case study, in particular, and have already led to the discovery of the multiply imaged SN H0pe. Considering their lens model-corrected SFRs, we estimate their intrinsic SN rates to be an extraordinary 1.8–65 yr^{-1} (core-collapse) and 0.2–6.4 yr^{-1} (Type Ia). Moreover, these massive starbursts typically have star-forming companions which are unaccounted for in this tally. We demonstrate a strong correlation between Einstein radius and typical time delays, with cluster lenses often exceeding several months (and therefore most favorable for high-precision H_0 inferences). A multivisit monitoring campaign with a sensitive infrared telescope (namely, JWST) is necessary to mitigate dust attenuation. Nevertheless, a porous interstellar medium and clumpy star formation in these extreme galaxies might produce favorable conditions for detecting SNe as transient point sources. Targeted campaigns of known lensed galaxies to discover new lensed SNe can greatly complement wide-area cadenced surveys. Increasing the sample size helps to realize the potential of SN time-delay cosmography to elucidate the Hubble tension through a single-step measurement, independent of other H_0 techniques.

Unified Astronomy Thesaurus concepts: Hubble constant (758); Starburst galaxies (1570); Strong gravitational lensing (1643); Supernovae (1668)

1. Introduction

Gravitationally lensed supernovae (glSNe) are invaluable cosmological tools that are finally now being discovered and leveraged to make unique, one-step measurements of the Hubble constant, H_0, describing the expansion rate of the Universe (S. H. Suyu et al. 2024). For multiply imaged lensed objects, the arrival of the different images is staggered in time due to: (i) the difference in path lengths along the different null geodesics; and (ii) the Shapiro effect (I. I. Shapiro 1964), by which the light rays experience disparate amounts of time dilation from the differing gravitational potential along their paths. The magnitude of this effect for galaxies at cosmological distances—typically of order hours to decades—is usually far too small to be detectable, given the timescales of Myr for galaxy-scale variations. However, with rapidly varying or transient signals, such as from quasars or supernovae (SNe), it is possible to capture and measure these lensing-induced time delays through light-curve monitoring. Through a technique now known as time-delay (TD) cosmography, which was first introduced by S. Refsdal (1964) (see also reviews by R. D. Blandford & R. Narayan 1992; T. Treu & P. J. Marshall 2016; T. Treu et al. 2022; S. Birrer et al. 2024), these delays may be inverted to infer distances within the Hubble flow, and therefore H_0. This is due

Original content from this work may be used under the terms of the Creative Commons Attribution 4.0 licence. Any further distribution of this work must maintain attribution to the author(s) and the title of the work, journal citation and DOI.

to the dependence of the time delays on a ratio of three angular-diameter distances (from the observer to the lens, from the observer to the source, and from the lens to the source; P. Schneider 1985), which in turn is proportional to H_0^{-1} (with minimal dependence on other cosmological parameters).

The "Hubble tension" between calculations of the Hubble constant H_0 still endures, despite an extraordinary number of measurements that have been put forth in the last two decades (see recent review by L. Verde et al. 2024). The primary conflict arises from the smaller value of $H_0 = 67.4 \pm 0.5\,\mathrm{km\,s^{-1}\,Mpc^{-1}}$ (Planck Collaboration et al. 2020) inferred from the cosmic microwave background within the standard ΛCDM model (also S. Aiola et al. 2020; T. Louis et al. 2025), relative to the larger values found from the local Universe (e.g., $H_0 = 73.0 \pm 1.0\,\mathrm{km\,s^{-1}\,Mpc^{-1}}$ from SH0ES; A. G. Riess et al. 2022). The latter measurements are predominantly determined through calibration of a distance ladder on cosmological scales, making use of indicators such as Type Ia supernovae (SNe Ia) in combination with, e.g., (i) Cepheid variable stars (e.g., A. G. Riess et al. 2022), (ii) the tip of the red giant branch (e.g., W. L. Freedman et al. 2019; G. S. Anand et al. 2024), or (iii) the J-region asymptotic giant branch (e.g., A. J. Lee et al. 2021; W. L. Freedman et al. 2025). Given the manifold challenges in this calibration (E. Mörtsell et al. 2022a, 2022b), there is a drastic need for independent and orthogonal measurements of H_0 that do not suffer from the same systematics.

One such example is the Megamaser Cosmology Project (M. J. Reid et al. 2009, 2013; D. W. Pesce et al. 2020), which enables a "single-rung" geometric distance inference through high-precision mapping of circumnuclear H_2O masers originating from accretion disks around active galactic nuclei (AGN) in low-z galaxies. Another, of course, is TD cosmography, which is capable of yielding a single-rung measurement well into the Hubble flow without hinging on the possible pitfalls from the usual distance ladder methods.[15]

TD cosmography has perhaps matured more quickly for lensed quasars, which are variable but offer the benefit of persistence that SNe lack (S. Birrer et al. 2020, 2024; K. C. Wong et al. 2020). Over 300 lensed quasars have been identified, most with image separations of only a few arcseconds and with time delays typically less than one year, although some (e.g., J. Fohlmeister et al. 2007, 2008; H. Dahle et al. 2015; J. A. Muñoz et al. 2022; K. Napier et al. 2023) have measured time delays using wide-separation cluster-lensed quasars (which have some advantages over galaxy-scale lenses and their systematic uncertainties; C. S. Kochanek 2020). However, inferring time delays from quasars requires extensive long-term or high-cadence monitoring for accurate measurements (F. Courbin et al. 2005, 2018; V. Bonvin et al. 2017), and can be plagued by microlensing (M. J. Irwin et al. 1989; H. J. Witt et al. 1995; P. L. Schechter et al. 2003; G. Vernardos et al. 2024), degeneracies and systematics in lens models (C. R. Keeton et al. 2000; L. V. E. Koopmans et al. 2003), and the well-known mass-sheet and mass-slope degeneracies (E. E. Falco et al. 1985; M. V. Gorenstein et al. 1988; J. Wambsganss & B. Paczynski 1994; C. S. Kochanek 2002; P. Schneider & D. Sluse 2013). While some of these challenges also affect TD cosmography with SNe, this approach has some distinct advantages. Their rapid and more predictable variation in brightness means that time delays can be measured with much shorter monitoring campaigns—even as little as a few hours of spectroscopy (W. Chen et al. 2024)—and with a level of precision and accuracy that is actually more affected by photometric uncertainties than by microlensing (e.g., J. D. R. Pierel & S. Rodney 2019; S. Huber et al. 2022; J. D. R. Pierel et al. 2024a).

Perhaps the most important systematic plaguing the TD cosmography approach for SNe at present is scarcity. SNe are inherently rare events—$\lesssim$1% of all stars will end their lifetimes in core-collapse supernovas (CCSNe). Since their duration above a survey's sensitivity limits is short-lived, especially at $z > 1$, their discovery essentially requires a not insignificant amount of luck. Strong gravitational lensing in the regime of producing multiple images is similarly quite rare (T. Treu 2010). While the lensing optical depth (probability of being lensed above a certain magnification threshold or lensed into more than one image) increases monotonically with source-plane redshift, this largely asymptotes above $z \gtrsim 2$ (e.g., S. Hilbert et al. 2007, 2008; A. Robertson et al. 2020). As a result, barely more than a handful of other multiply imaged lensed SNe have been discovered in the last decade since S. Refsdal was first identified behind the MACS J1149.6+2223 galaxy cluster (P. L. Kelly et al. 2015, 2016; C. Grillo et al. 2018; H_0 measurements in P. L. Kelly et al. 2023a; C. Grillo et al. 2024). Since then, three other glSNe suitable for TD cosmography have been discovered: SN H0pe behind the PLCK G165.7+67.0 cluster (B. L. Frye et al. 2023, 2024), and the pair of SN Requiem (S. A. Rodney et al. 2021) and SN Encore (J. D. R. Pierel et al. 2024b), both within the same massive host galaxy lensed by MACS J0138.0-2155 and separated by 2.5 yr in the galaxy's rest frame. The analysis of SN H0pe, the first confirmed glSN Ia used for TD cosmography, recently produced a new H_0 measurement at ∼10% precision (M. Pascale et al. 2025). This work also introduced a new weighting scheme for the seven independently constructed lens models according to their ability to accurately predict observables such as magnifications, made possible by H0pe's nature as a standardizable candle. The first H_0 results from SN Encore have been published (S. Ertl et al. 2025; S. Suyu et al. 2025; J. D. R. Pierel et al. 2026), and now there is also hope for a precise measurement from SN Requiem's return a decade later in 2026–2027 (HST program GO-18069).

Upcoming wide-area surveys such as the Vera C. Rubin Observatory's Legacy Survey of Space and Time (LSST; LSST Science Collaboration et al. 2009) promise to reveal $\sim$50–100 glSNe $\mathrm{yr^{-1}}$ (N. Arendse et al. 2024; S. Bag et al. 2024; A. Sainz de Murieta et al. 2024; A. Melo et al. 2025), but not all of these will be discovered sufficiently early to follow up with light-curve monitoring for the purposes of TD cosmography. In addition, many of the glSNe behind galaxy-scale deflectors will have time delays that are too short to yield meaningful precision on H_0, as in the case of iPTF16geu ($z = 0.409$; A. Goobar et al. 2017). Moreover, in the pessimistic scenario, currently active facilities such as the Zwicky Transient Facility (E. Bellm 2014) were expected to yield at least one glSN per year, but only one was identified in four years (SN Zwicky at $z = 0.354$; A. Goobar et al. 2023; J. D. R. Pierel et al. 2023), with few other compelling candidates (M. R. Magee et al. 2023; A. Sagués Carracedo et al. 2024; see also P. Craig et al. 2024). Still, the next decade

[15] To be clear, this technique does not rely on the nature of SNe Ia as "standardizable candles" like other late-Universe efforts (although this property may assist in more objectively assessing the accuracy of various lens models; M. Pascale et al. 2025). SNe are simply a useful transient source by which time delays may be measured, revealing the underlying cosmology.

is likely to see TD cosmography with glSNe mature more fully and reach a competitive precision on H_0, closer to 1% than 10% (T. Treu et al. 2022).

What, then, is the best strategy at present for discovering "live" glSNe[16]? One answer might come from remarking that some of the recent discoveries have been identified behind well-studied lensing clusters. These include two of the famous Hubble Frontier Fields: S. Refsdal behind MACS J1149.6+2223 (P. L. Kelly et al. 2015) and a $z \approx 3$ CCSN behind A370 (W. Chen et al. 2022). There is undoubtedly an observational bias here, given the attention these fields receive, resulting in a more well-sampled cadence, and the presence of numerous lens models to identify multiple imaging (M. Bronikowski et al. 2025). Yet, these massive lensing clusters also provide sizable magnification for a large number of background sources (e.g., A. Gal-Yam et al. 2002; V. Stanishev et al. 2009; T. Petrushevska et al. 2016, 2018a, 2018b; T. Petrushevska 2020). However, SN H0pe, SN Requiem, and SN Encore were all identified within high-mass host galaxies lensed by less massive, previously lesser-known clusters. These discoveries were facilitated not necessarily by the extraordinary nature of the foreground but more so of the background lensed host galaxies.

A targeted search for glSNe in known lensed galaxies that are very massive or have a high star formation rate (SFR) (or both) is not an entirely novel idea. Y. Shu et al. (2018) estimated that monitoring a sample of >100 galaxy-scale lensed star-forming galaxies would yield rates of ~3 combined CCSN and SN Ia events per year (Y. Shu et al. 2021), reaching a greater efficiency than a blind search. A targeted strategy also provides greater confidence that any discovered SNe are in fact lensed (see also B. W. Holwerda et al. 2021). Here, we modify the approach to encompass a much smaller sample, but with commensurately larger rates of star formation. There is some difficulty in identifying sufficient numbers of starburst galaxies (with high intrinsic rates of SNe) that are lensed into multiple images. One possible approach is to monitor samples of known lensed dusty star-forming galaxies (DSFGs), also referred to as submillimeter galaxies (SMGs) which now number in the hundreds (M. Giulietti et al. 2024), since these objects are inferred to form stars at prodigious rates of 300–1000 $M_\odot\,\mathrm{yr}^{-1}$ (or even greater). The prevailing selection method for this population is unique, relying essentially on submillimeter flux alone (A. W. Blain 1996; F. Perrotta et al. 2002; M. Negrello et al. 2010, 2017), as opposed to methods that identify distorted lensing morphologies or peaks in foreground mass density or Sunyaev–Zel'dovich effect signal.

As an application of this tactic, we examine in particular the set of lensed DSFGs identified from Planck, which is perhaps most well suited for this experiment due to its all-sky coverage. For now, we consider the ~30 members of the Planck All-Sky Survey to Analyze Gravitationally-lensed Extreme Starbursts (PASSAGES; K. C. Harrington et al. 2016; D. A. Berman et al. 2022; P. S. Kamieneski et al. 2024a), some of which were also identified independently through Herschel follow up (R. Cañameras et al. 2015; Planck Collaboration et al. 2015). Of these, 21 objects (summarized in Table 1) have the information necessary to compute expected glSN rates (Sections 2.4 and 3.1). P. S. Kamieneski et al. (2024a) determined that the median delensed (i.e., intrinsic) infrared luminosity for PASSAGES exceeded $10^{13}\,L_\odot$, qualifying them as hyperluminous infrared galaxies (HyLIRGs). Nonetheless, the dust geometry of such extreme HyLIRGs remains quite uncertain at high-z. Any SNe are likely to be attenuated by dust in even the best-case scenario, so near-infrared sensitivity is paramount.

HyLIRGs such as these are often signposts of significant overdense regions (e.g., N. Foo et al. 2025). While we consider primarily the contribution to the SN rate from the primary starburst galaxies, there is a high likelihood of other star-forming objects at the same redshift that might also fall into the strongly lensed portion of the source plane, further boosting the chances of identifying lensed transients in these fields. This is also borne out in part with the discovery of SN H0pe behind the lensing cluster G165.7+67.0, which was itself identified through its amplification of one of the PASSAGES DSFGs. Initial JWST/NIRCam imaging of the field through the Prime Extragalactic Areas for Reionization and Lensing Science program (R. A. Windhorst et al. 2023) revealed the SN Ia not within the giant arc of lensed DSFGs but in a highly magnified arc nearby in projection. Both this host galaxy and the DSFGs were found to be members of respective photometric-redshift overdensities at $z = 1.78$ and $z = 2.24$ (B. L. Frye et al. 2024).

This work is organized as follows. In Section 2, we detail our novel approach to deriving forecasts for the intrinsic and observer-frame rates of SNe in HyLIRGs, using the PASSAGES fields as an example. In Section 3, we discuss our inference of SFRs (both obscured and unobscured modes), lensing multiplicities, and the core-collapse and degenerate white dwarf SN rates that result from these inferences. We also examine the expected typical time delays and draw a connection to the angular separation between images. In Section 4, we summarize our findings and reflect on the feasibility of our proposed approach in making a meaningful contribution to the rather saturated industry of deriving H_0 constraints. Throughout, we adopt a fiducial ΛCDM concordance cosmology of $\Omega_m = 0.3$, $\Omega_\Lambda = 0.7$, and $H_0 = 70\,\mathrm{km\,s^{-1}\,Mpc^{-1}}$.

2. Observations and Methods

2.1. Case Study Sample Selection: PASSAGES

In this work, we aim to forecast the expected rates of SNe from strongly lensed DSFGs at $z > 1$. Lensed DSFGs are efficiently selected through their submillimeter flux owing to a steep drop-off in number counts (A. W. Blain 1996), such that an extragalactic source brighter than 100 mJy at 500 μm is $\gtrsim$30 times more likely to be lensed than unlensed (M. Negrello et al. 2017). However, they are still rare objects, with a modeled all-sky number density of $0.09 \pm 0.05\,\mathrm{deg}^{-2}$ for $S_{500\mu\mathrm{m}} > 80$ mJy, while observations suggest up to $\sim 0.3\,\mathrm{deg}^{-2}$ (C. Sedgwick et al. 2025, and references therein including M. Negrello et al. 2010; R. S. Bussmann et al. 2013; J. L. Wardlow et al. 2013; M. Negrello et al. 2014, 2017; T. J. L. C. Bakx et al. 2018; S. A. Urquhart et al. 2022; E. Borsato et al. 2024). This model predicts 3600 ± 1800 such sources to exist in the entire sky (increasing by a factor of ~40 if the threshold is lowered by a factor of 10; T. J. L. C. Bakx et al. 2024b; C. Sedgwick et al. 2025), but so far only a few hundred such objects have been uncovered (e.g., M. Giulietti et al. 2024). Euclid's Wide Survey (Euclid Collaboration et al. 2022) is expected to be sensitive to several thousand.

[16] Here, "live" glSNe draws a distinction from those discovered after the SN has faded in all images, only apparent through its disappearance in a second epoch of observation, and therefore not suitable for monitoring to infer H_0.

Table 1
Estimated Intrinsic and Observable Rates of SNe in a Subset of PASSAGES

ID	z_s	μ	$\mathrm{SFR}_{\mathrm{IR,intr.}}$ ($M_\odot\ \mathrm{yr}^{-1}$)	f_{unobsc}[a] (%)	$R_{\mathrm{CC}}(\mathrm{SFR}_{\mathrm{IR}})$ (yr^{-1})	R_{Ia} (yr^{-1})	$\mathcal{N}_{\mathrm{eff}}$	$\mathcal{R}_{\mathrm{CC,obs}}$ (yr^{-1})	$\mathcal{R}_{\mathrm{Ia,obs}}$ (yr^{-1})	References
PJ0116−24	2.125	≈17	1490 ± 400	≈32%[b]	15.5 ± 4.2	1.5 ± 0.4	2.3 ± 0.5	3.6 ± 0.9	1.1 ± 0.4	(1)
PJ0143−01	1.096	7.1 ± 2.2	170 ± 50	20% ± 10%	1.8 ± 0.5	0.2 ± 0.1	2.3 ± 0.5	0.4 ± 0.2	0.2 ± 0.1	(2) μ (3) SFR
PJ0209+00	2.554	10.5 ± 3.7	2030 ± 820	20% ± 10%	21.1 ± 8.5	2.1 ± 0.8	2.2 ± 0.4	2.6 ± 1.8	1.3 ± 0.6	(2) μ (4) SFR
PJ0226+23	3.120	28.2 ± 11.3	1020 ± 470	20% ± 10%	10.6 ± 4.9	1.0 ± 0.5	4.0 ± 0.8	2.1 ± 1.5	1.0 ± 0.5	(2) μ (3) SFR
PJ0305−30	2.263	2.2 ± 0.6	6290 ± 1850	20% ± 10%	65 ± 19	6.4 ± 1.9	2.0 ± 0.4	8.0 ± 4.9	3.9 ± 1.4	(2) μ (3) SFR
PJ0748+59	2.755	≈15	920 ± 250	20% ± 10%	9.6 ± 2.6	0.9 ± 0.3	3.0 ± 0.6	1.5 ± 0.9	0.8 ± 0.3	(5) μ (3) SFR
PJ0846+15	2.664	7.7 ± 1.5	5200 ± 2600	20% ± 10%	54 ± 27	5.3 ± 2.6	1.5 ± 0.3	4.4 ± 3.3	2.2 ± 1.2	(6) μ (3) SFR
PJ1053+60	3.549	≈24	710 ± 200	20% ± 10%	7.4 ± 2.1	0.7 ± 0.2	3.0 ± 0.6	1.0 ± 0.6	0.5 ± 0.2	(7) μ (3) SFR
PJ1053+05	3.005	7.6 ± 0.7	2610 ± 590	20% ± 10%	27.1 ± 6.1	2.7 ± 0.6	3.0 ± 0.6	4.1 ± 2.4	2.0 ± 0.6	(2) μ (4) SFR
PJ1127+46	1.303	4.5 ± 0.6	590 ± 120	20% ± 10%	6.1 ± 1.2	0.6 ± 0.1	2.0 ± 0.4	1.1 ± 0.6	0.5 ± 0.2	(2) μ (3) SFR
PJ1127+42	2.236	16.4 ± 3.0	720 ± 110	≈ 31%	7.5 ± 1.1	0.7 ± 0.1	1.3 ± 0.3	0.9 ± 0.2	0.3 ± 0.1	(8) μ (4) SFR
PJ1138+32	2.019	2.8 ± 0.4	910 ± 190	20% ± 10%	9.5 ± 2.0	0.9 ± 0.2	2.0 ± 0.4	1.3 ± 0.7	0.6 ± 0.2	(2) μ (3) SFR
PJ1139+20	2.858	4.8 ± 1.1	2660 ± 750	20% ± 10%	27.7 ± 7.8	2.7 ± 0.8	3.0 ± 0.6	4.3 ± 2.6	2.1 ± 0.7	(2) μ (3) SFR
PJ1322+09	2.068	≈20	460 ± 120	20% ± 10%	4.8 ± 1.2	0.5 ± 0.1	6.0 ± 1.2	1.9 ± 1.1	0.9 ± 0.3	(5) μ (3) SFR
PJ1326+33	2.951	4.3 ± 0.6	1860 ± 470	20% ± 10%	19.3 ± 4.9	1.9 ± 0.5	2.0 ± 0.4	2.0 ± 1.2	1.0 ± 0.3	(2) μ (3) SFR
PJ1329+22	2.040	11 ± 2	1380 ± 110	20% ± 10%	14.4 ± 1.1	1.4 ± 0.1	2.5 ± 0.5	2.4 ± 1.3	1.2 ± 0.3	(6) μ (3) SFR
PJ1336+49	3.254	8.3 ± 3.1	2310 ± 990	20% ± 10%	24 ± 10	2.4 ± 1.0	2.0 ± 0.4	2.3 ± 1.6	1.1 ± 0.5	(2) μ (3) SFR
PJ1446+17	1.084	3.9 ± 0.7	710 ± 180	20% ± 10%	7.4 ± 1.9	0.7 ± 0.2	3.3 ± 0.7	2.4 ± 1.4	1.2 ± 0.4	(2) μ (3) SFR
PJ1449+22	2.153	10.1 ± 5.2	1050 ± 580	20% ± 10%	10.9 ± 6.0	1.1 ± 0.6	4.0 ± 0.8	2.8 ± 2.1	1.4 ± 0.8	(2) μ (3) SFR
PJ1607+73	1.482	6.8 ± 1.7	220 ± 110	20% ± 10%	2.3 ± 1.1	0.2 ± 0.1	2.7 ± 0.5	0.5 ± 0.4	0.2 ± 0.1	(2) μ (4) SFR
PJ2313+01	2.217	6.1 ± 1.2	1060 ± 310	20% ± 10%	11.0 ± 3.2	1.1 ± 0.3	3.7 ± 0.7	2.5 ± 1.5	1.2 ± 0.4	(2) μ (3) SFR

Notes.
[a] Unobscured SFR estimated using the adopted f_{unobsc}, except for PJ0116-24 (D. Liu et al. 2024) and PJ1127+42 (G165), which are estimated directly from Hα (B. L. Frye et al. 2024) following correction from the measured Balmer decrement. For G165, we assume that the f_{unobsc} for Arc 1 (≈31%) applies also for its counterpart, Arc 3.
[b] Derived using $\mathrm{SFR}_{\mathrm{H}\alpha,\mathrm{corr}} = 470 \pm 60\ M_\odot\ \mathrm{yr}^{-1}$ (D. Liu et al. 2024).
References for SFR and μ estimates: (1) D. Liu et al. (2024); (2) P. S. Kamieneski et al. (2024a) (3) D. A. Berman et al. (2022); (4) K. C. Harrington et al. (2016); (5) P. Kamieneski et al. (2026, in preparation); (6) N. Foo et al. (2025); (7) Q. D. Wang et al. (2024); (8) P. S. Kamieneski et al. (2024b); (9) A. Díaz-Sánchez et al. (2017).

For now, while Planck's surveys reach shallower depths than Herschel, its wide-area coverage has been an asset for identifying the very brightest lensed DSFGs in the sky (T. Trombetti et al. 2021). As discussed by P. S. Kamieneski et al. (2024a), there is a complex balance between their intrinsic luminosities and their magnifications: HyLIRGs tend to have larger sizes to match their higher luminosities (in line with the Eddington limit; P. S. Kamieneski 2024), while size bias leads to more strongly magnified objects correlating with more compact sizes (Y. D. Hezaveh et al. 2012). Together, this means that candidates with apparent luminosities $\mu_{\mathrm{IR}}\mathrm{L}_{\mathrm{IR}} \gtrsim 10^{14}\,L_\odot$ tend to still have intrinsic $L_{\mathrm{IR}} \gtrsim 10^{12.5}\,L_\odot$. For this reason, the greater submillimeter fluxes of Planck-identified lensed DSFGs are not simply the result of higher magnifications alone. They are thus among the best candidates for high rates of glSNe given their high SFRs. Moreover, their lower median redshift than lensed DSFGs identified in the millimeter regime (e.g., with the South Pole Telescope; A. Weiss et al. 2013) lends well to greater ease in detecting glSNe in the observed-frame near-infrared.

2.2. Determining the Expected Value of Image Multiplicity

A galaxy that crosses the caustic network will have different parts of the source plane lensed into varying numbers of multiple images. In the canonical lensing example of a singular isothermal ellipsoid, an astroid tangential caustic encloses a region with an image multiplicity of four (excluding demagnified images), whereas the region between the tangential caustic and the elliptical radial caustic is lensed into two images, and structures exterior to the radial caustic are weakly lensed into only a single image. For cluster-scale lenses, which have larger source-plane areas inside the caustics, it is more likely for most of a galaxy's light to be contained within a region with constant image multiplicity. On the other hand, galaxy-scale lenses have much tighter caustic loci, so galaxies can easily cross caustics and have two (or even more) different image multiplicities of the source.

The lensing multiplicity of a galaxy has a direct bearing on the average rate of SNe that can be observed on Earth. To account for this, we introduce the concept of effective multiplicity, $\mathcal{N}_{\mathrm{eff}}$, which is the average multiplicity weighted by the distribution of star formation. We define it as

$$\mathcal{N}_{\mathrm{eff}} \equiv \sum_n \left[n \cdot \frac{\mathrm{SFR}_n}{\mathrm{SFR}} \right] \tag{1}$$

for the different multiplicities n, where SFR_n is the total SFR within the region of multiplicity n. This calculation is illustrated for a singular isothermal ellipsoid lens (with a large axis ratio) in a cartoon in Figure 1. $\mathcal{N}_{\mathrm{eff}}$ can also be functionally expressed as a pixel-based summation,

$$\mathcal{N}_{\mathrm{eff}} \equiv \frac{\sum_{i,j} N_{i,j}\mathrm{SFR}_{i,j}}{\sum_{i,j} \mathrm{SFR}_{i,j}} \tag{2}$$

where $\mathrm{SFR}_{i,j}$ and $N_{i,j}$ are the SFR and multiplicity, respectively, at pixel (i, j).

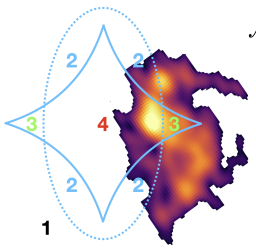

$$\mathcal{N}_{\rm eff} = \sum_n \left[n \cdot \frac{\rm SFR_n}{\rm SFR} \right]$$
$$= 1 \cdot {\rm SFR}(N=1)/{\rm SFR} \approx 1 \cdot 0.65$$
$$+ 2 \cdot {\rm SFR}(N=2)/{\rm SFR} \approx 2 \cdot 0.05$$
$$+ 3 \cdot {\rm SFR}(N=3)/{\rm SFR} \approx 3 \cdot 0.05$$
$$+ 4 \cdot {\rm SFR}(N=4)/{\rm SFR} \approx 4 \cdot 0.25$$
$$\approx 1.9$$

Figure 1. Cartoon schematic demonstrating the calculation of effective multiplicity $\mathcal{N}_{\rm eff}$ per Equation (1), using an ALMA 870 μm image of the unlensed DSFG ALESS 112.1 as an example (J. A. Hodge et al. 2019). Mock caustic curves from an imaginary lensing galaxy are overlaid (radial = dashed, tangential = solid). Put simply, $\mathcal{N}_{\rm eff}$ is the weighted average of multiplicities (n = 1, 2, 3,...), where the weights are the respective portions of the total SFR.

2.3. ALMA 1 mm Continuum and VLA 6 GHz

To infer a map of SFR to compute $\mathcal{N}_{\rm eff}$ with the information available for the majority of PASSAGES, we rely on the 1mm dust continuum observed with the Atacama Large Millimeter/submillimeter Array (ALMA), by which we apportion the total infrared spectral energy distribution (SED) derived SFR (primarily from K. C. Harrington et al. 2016; D. A. Berman et al. 2022). For northern-declination sources not covered in these observations, we instead use 6 GHz (5 cm) continuum imaging from the Karl G. Jansky Very Large Array (VLA) in A configuration, with angular resolutions relatively close to the ALMA images. The 6 GHz images are largely correlated with the dust continuum through the radio–far-infrared correlation (e.g., J. J. Condon 1992). These observations are described in detail in Sections 2.4 and 2.5 of P. S. Kamieneski et al. (2024a), with images shown in their Figure 2.

We use these observations to map the source-plane spatial distribution of $\rm SFR_{IR}$ (as inferred from unresolved far-infrared photometry, the source of which is specified for each target in Table 1). Since the star formation is likely dominated by the obscured mode probed by $\rm SFR_{IR}$, the distribution $\Sigma_{\rm SFR_{IR}}$ is our best estimate of the 2D probability density function of CCSNe (e.g., M. Miluzio et al. 2013). While slightly less direct, this is also likely to closely match the spatial distribution of SNe Ia (especially if one assumes that $\Sigma_{\rm SFR}$ correlates with the distribution of stellar mass, $\Sigma_\star$; e.g., W. M. Baker et al. 2022). Of course, the observed distribution of SNe is more complex, and depends on dust geometry, but for the purpose of computing $\mathcal{N}_{\rm eff}$, $\Sigma_{\rm SFR_{IR}}$ should suffice. Nonetheless, given the highly stochastic nature of SNe, even for galaxies with very high SFRs, and imperfections in the lens models, we adopt a conservative fractional uncertainty[17] of 20% on $\mathcal{N}_{\rm eff}$. The achieved resolutions for the ALMA and VLA observations ranged from $\theta \approx 0\farcs4$–$0\farcs8$ and $\theta \approx 0\farcs3$–$0\farcs7$, respectively. While higher-resolution observations (e.g., spatially resolved SED fitting with JWST) would improve the fidelity of $\mathcal{N}_{\rm eff}$, the location of the caustic network from lens models and systematics of SED fitting dominate the uncertainty at present.

[17] This uncertainty can be very roughly approximated as the fraction of a galaxy's star-forming area that is within the 1σ uncertainty on the caustic's location, multiplied by the relative change in multiplicity on either side of the caustic. In a canonical case of a galaxy straddling a caustic curve separating regions of double- versus quad-imaging, this would be $\Delta N = 2$ from the $N = 2$ to $N = 4$ region, with average $N \sim 3$. For a source-plane positional uncertainty of $\sim 0\farcs1$ and a typical source-plane size of $\sim 0\farcs4$ for PASSAGES (P. S. Kamieneski et al. 2024a), the typical uncertainty thus becomes $\sigma_{\mathcal{N}_{\rm eff}}/\mathcal{N}_{\rm eff} \sim (0.1/0.4) \cdot (4-2)/3 \sim 20\%$.

There is some concern that heavily dust-obscured AGN might contribute in the radio (J. L. Donley et al. 2005; A. Del Moro et al. 2013; I. Delvecchio et al. 2017), thus biasing the calculation of $\mathcal{N}_{\rm eff}$. However, P. S. Kamieneski et al. (2024a) found that the PASSAGES DSFGs did not have obvious evidence of radio-loud AGN manifesting as an excess in spatially integrated radio continuum relative to far-infrared, suggesting that this bias is not likely to have a sizable effect.

2.4. Estimating the Obscured and Unobscured SFR

2.4.1. The Situation at Low-z versus z > 2

CCSNe have been discovered successfully in low-z luminous infrared galaxies (LIRGs) in the near-infrared within projected radii <1 kpc (F. Mannucci et al. 2003; S. Mattila et al. 2007; E. Kankare et al. 2008, 2012; M. Miluzio et al. 2013; E. C. Kool et al. 2018; J. E. Jencson et al. 2019; O. D. Fox et al. 2021; E. Kankare et al. 2021; M. Pérez-Torres et al. 2021). These include some radio SNe and SN remnants found through very long baseline interferometry (C. J. Lonsdale et al. 2006; I. Martí-Vidal et al. 2007; R. Parra et al. 2007; M. A. Pérez-Torres et al. 2009; M. Bondi et al. 2012; E. Varenius et al. 2019). On the other hand, some campaigns have yielded zero, or at least drastically fewer than expected, detected events for starbursts and ultraluminous infrared galaxies (ULIRGs), including G. Cresci et al. (2007) with Hubble Space Telescope (HST)/NICMOS, or P. Väisänen et al. (2008) with adaptive optics-assisted Very Large Telescope (VLT) imaging. I. Mäntynen et al. (2025) recently found that ≈90% of CCSNe in local LIRGs might be missed if attenuations of only up to $A_V < 3$ mag are detectable. Even if hypothetically sensitive to extremely high values of $A_V \gtrsim 40$, the authors obtain an undetectable fraction $\gtrsim$ 50% owing to the concentrated distribution of dust and star formation in local LIRGs. O. D. Fox et al. (2021) emphasized the importance of a stable, symmetric, high-resolution point-spread function in the near-infrared (as achieved with space-based facilities) in order to combat this high concentration.

This might paint a dire picture for executing successful campaigns at high-z, although clever workarounds are possible. For example, H. Yan et al. (2018) demonstrated that the presence of SNe may be revealed through variability in the integrated near-infrared light of a galaxy (at the time with Spitzer). Yet, for very high-SFR galaxies ($\gtrsim 300\,M_\odot\,{\rm yr}^{-1}$, or $\gtrsim$3 CCSNe $\rm yr^{-1}$), the signal from such variability may be difficult to discern due to overlapping SNe and a higher near-infrared background. However, there also appear to be key distinctions between the typical structures of high-z HyLIRGs and the LIRGs/ULIRGs in the low-z Universe. The typical star-dust geometry of DSFGs and starburst galaxies remains a matter of ongoing research, which of course has implications for the detectability of SNe. In particular, the presence of unobscured UV-bright sightlines in DSFGs may be responsible for bluer UV slopes $\beta_{\rm UV}$, resulting in the observed deviation from the IRX–β relation (G. R. Meurer et al. 1999) where IRX$\equiv L_{\rm IR}/L_{\rm UV}$ is the infrared excess (e.g., L. Cortese et al. 2006; M. Boquien et al. 2009; C. M. Casey et al. 2014b; A. L. Faisst et al. 2017; M. Safarzadeh et al. 2017; D. Narayanan et al. 2018; L. Liang et al. 2021). In essence, the exceptional rate of SNe occurring per year in each of the PASSAGES galaxies (Table 1) is likely to result in a very porous interstellar medium (ISM), especially considering the

groundwork laid by pre-SN feedback (W. E. Lucas et al. 2020; M. Chevance et al. 2022; E. J. Watkins et al. 2023). In local star-forming galaxies, for example, the timescale for dispersal of molecular clouds is of order 1–5 Myr, comparable to or shorter than the lifetime of massive CCSN progenitors (M. Chevance et al. 2020). SNe are likely to occur within an inhomogeneous medium and further contribute to this through compression of swept-up shells and rarefied bubbles (e.g., C. Clarke & M. S. Oey 2002; C.-G. Kim & E. C. Ostriker 2015). This ISM structure, in turn, favors the ability to observe SNe, even in dusty environments.

Local ULIRGs often host extremely concentrated starburst regions (although as K. B. W. McQuinn et al. 2012 point out, this may be partially a selection bias). This high concentration reaches an extreme with compact obscured nuclei, or CONs (which have sizes of 10–100 pc and very high attenuations of $A_V \gtrsim 10$; K. Sakamoto et al. 2013; S. Aalto et al. 2015; N. Falstad et al. 2021). At Cosmic Noon ($z \sim 1$–3), their more luminous counterparts sustain high rates of star formation over the scale of several kpc (W. Rujopakarn et al. 2011; J. A. Hodge et al. 2016, 2019; K. C. Harrington et al. 2021; P. S. Kamieneski et al. 2024a, 2024b; I. Mitsuhashi et al. 2024; M. Polletta et al. 2024), often in clumps resulting from gravitational instabilities in gas-rich disks (A. Immeli et al. 2004; K. Tadaki et al. 2018; D. Liu et al. 2024; A. L. Faisst et al. 2025; S. Fujimoto et al. 2025; B. S. Kalita et al. 2025) that are continually replenished through accretion (F. Bournaud et al. 2007; A. Dekel et al. 2009). For example, under assumption that the dust masses of DSFGs are uniformly distributed within their half-light radii, J. M. Simpson et al. (2017) estimated extreme attenuation of order $A_V \sim 500$. However, this is unlikely to be accurate for a typical sightline in a less simplistic ISM structure that has a mixed star-dust geometry, is clumpy and multiphase, and carved by stellar feedback. Moreover, the finding of compact regions of dust emission (e.g., B. Gullberg et al. 2019) suggests that the outskirts of DSFGs are likely to have clearer lines of sight, regardless of the true porosity of the dusty ISM.

In addition, the high rates of star formation likely lend well to an increased rate of star cluster formation, and thus a better sampling of the high-mass end of the cluster mass function. For example, super star clusters (SSCs) are preferentially found in intense starburst regions, as exemplified by M82 and the Antennae Galaxies (e.g., L. J. Smith & J. S. Gallagher 2001; S. Mengel et al. 2002; R. de Grijs et al. 2003; B. C. Whitmore et al. 2010; S. T. Linden et al. 2017; K. L. Emig et al. 2020; R. C. Levy et al. 2024). If much of the star formation of DSFGs is concentrated in SSCs, which are progenitors of massive globular clusters, then their strong stellar feedback may contribute to clearing sightlines that both allows for Lyman continuum leakage (e.g., A. Bik et al. 2018; M. Pascale et al. 2023; Z. Ji et al. 2025) and the escape of less-attenuated optical light from SNe (e.g., E. Leitet et al. 2013; N. Roy et al. 2025).

2.4.2. Adopting a Fraction of Unobscured SFR

Hα SFRs are typically significantly less than those derived from the infrared. This discrepancy is primarily resolved after applying a Balmer decrement extinction correction to the Hα-derived value (L. J. Kewley et al. 2002; T. Takata et al. 2006; H. Domínguez Sánchez et al. 2012; N. Timmons et al. 2015; A. Puglisi et al. 2016; D. Liu et al. 2024), although not in all cases (C.-C. Chen et al. 2020). For the D. Calzetti et al. (2000) attenuation curve, $\mathrm{SFR}_{\mathrm{H}\alpha}$ is corrected as

$$\mathrm{SFR}_{\mathrm{H}\alpha,\mathrm{corr}} = \mathrm{SFR}_{\mathrm{H}\alpha} \cdot 10^{0.4 \cdot E(B-V)_{\mathrm{neb}} \cdot k'(\mathrm{H}\alpha)} \quad (3)$$

where $k'(0.656\,\mu\mathrm{m}) \approx 3.325$ and $E(B-V)_{\mathrm{neb}}$ is the color excess inferred from emission lines,

$$E(B-V)_{\mathrm{neb}} \approx 1.97 \cdot \log_{10}\left[\frac{L_{\mathrm{H}\alpha}/L_{\mathrm{H}\beta}}{2.86}\right] \quad (4)$$

for case B recombination (D. E. Osterbrock & G. J. Ferland 2006). Inherently, the strong attenuation of DSFGs has made it difficult to recover multiple Balmer lines. In a composite spectrum of 31 DSFGs in the COSMOS field, C. M. Casey et al. (2017) found a median Balmer decrement of 21.0 ± 2.4, yielding $E(B-V) = 1.7 \pm 0.1$ or $A_V = 6.9 \pm 1.4$ (using $R_V = 4.05 \pm 0.80$). This is higher than observed even for local ULIRGs on global scales (e.g., V. Wild et al. 2011). More recently, in a sample of typical DSFGs at $z \sim 2$–3, O. R. Cooper et al. (2025) found consistency with the shape of the D. Calzetti et al. (2000) attenuation curve, and $A_V \sim 3$–4, through combination of Balmer and Paschen lines obtained with JWST/NIRSpec.

Since some star formation is likely to be hosted in regions with dust obscuration strong enough such that no Hα emission would be detectable, these Balmer decrements are biased low (A. Puglisi et al. 2017). Extinction-corrected $\mathrm{SFR}_{\mathrm{H}\alpha}$ estimates are likely to give a more realistic assessment of the observable rates of SNe, however. Therefore, in our analysis, we introduce an unobscured fraction $f_{\mathrm{unobsc}} \equiv \mathrm{SFR}_{\mathrm{unobsc}}/\mathrm{SFR}_{\mathrm{IR}}$($\sim \mathrm{SFR}_{\mathrm{H}\alpha,\mathrm{corr}}/\mathrm{SFR}_{\mathrm{IR}}$). For example, V. Olivares et al. (2016) found this fraction to be <30% in $z \sim 2$ SMGs (an upper limit since their Hα SFRs are not corrected for extinction). In other words, the discrepancy between the extinction-corrected $\mathrm{SFR}_{\mathrm{H}\alpha,\mathrm{corr}}$ and $\mathrm{SFR}_{\mathrm{IR}}$ is a quantification of how much star formation is hosted in regions of extreme attenuation (from which neither Hβ nor Hα may be detected). As we discuss further in Section 3.1, f_{unobsc} is primarily introduced here as an upper limit on what fraction of SNe might conceivably be observed; the actual rate is observation-dependent and will be consistent with some value between the uncorrected and corrected $\mathrm{SFR}_{\mathrm{H}\alpha}$ values.

For the PASSAGES sample itself, two members already have measurements of the Balmer decrement. For the pair of DSFGs PJ1127+42 at $z = 2.24$ (comprising Arcs 1abc, 3abc, 4abc, and 6abc lensed by the G165.7+67.0 cluster), B. L. Frye et al. (2024) found a value of $E(B-V) = 0.85 \pm 0.25$ through NIRSpec observations (corresponding to a Balmer decrement of 7.7 ± 2.3 and $A_V = 3.4 \pm 1.2$). This yields a correction of $\log_{10}(\mathrm{SFR}_{\mathrm{H}\alpha}/\mathrm{SFR}_{\mathrm{H}\alpha,\mathrm{corr}}) = -1.1 \pm 0.3$, such that the demagnified $\mathrm{SFR}_{\mathrm{H}\alpha,\mathrm{corr}} \approx 100^{+200}_{-70}\,M_\odot\,\mathrm{yr}^{-1}$ for Arc 1 only. Given that $\mathrm{SFR}_{\mathrm{IR}} = 320 \pm 70\,M_\odot\,\mathrm{yr}^{-1}$ for the same object (P. S. Kamieneski et al. 2024b), this gives $f_{\mathrm{unobsc}} \approx 31\%$. We adopt this fraction for the entire arc complex (Arcs 1, 3, 4, and 6, per notation from B. L. Frye et al. 2019), which all lies at $z \approx 2.24$ (R. Cañameras et al. 2018; P. S. Kamieneski et al. 2024b). Similarly, for PJ0116-24 ($z = 2.13$), D. Liu et al. (2024) derived a color excess through Balmer decrement of $E(B-V) = 0.95 \pm 0.13$ with VLT/ERIS observations (Balmer decrement 8.7 ± 1.3; $A_V = 3.9 \pm 0.9$), suggesting $\log_{10}(\mathrm{SFR}_{\mathrm{H}\alpha}/\mathrm{SFR}_{\mathrm{H}\alpha,\mathrm{corr}}) = -1.3 \pm 0.2$ and $\mathrm{SFR}_{\mathrm{H}\alpha,\mathrm{corr}} = 470 \pm 60\,M_\odot\,\mathrm{yr}^{-1}$ and $f_{\mathrm{unobsc}} \approx 32\%$. In this work, for objects

without these Balmer decrement measurements at present, we adopt a range of $f_{\rm unobsc} = 20\% \pm 10\%$ in Table 1 (see also, e.g., A. M. Swinbank et al. 2004; C. Cheng et al. 2020; C.-C. Chen et al. 2020).

This might at first seem to run counter to the results of K. E. Whitaker et al. (2017) that $f_{\rm obsc} \equiv {\rm SFR_{IR}}/{\rm SFR_{UV+IR}}$ increases continually for higher SFRs and stellar masses (exceeding 90% for massive galaxies $\log(M/M_\odot) > 10.5$).[18] Higher dust obscuration may be due to elevated surface densities of both star formation and gas (which are themselves correlated; M. Schmidt 1959; R. C. J. Kennicutt 1998). However, $\Sigma_{\rm SFR}$ does not seem to increase strongly with $L_{\rm FIR}$. The size–luminosity relation found by S. Fujimoto et al. (2017) for $11 \lesssim \log(L_{\rm FIR}/L_\odot) \lesssim 13$, $R_e \propto L_{\rm FIR}^{0.28}$, implies a weak dependence of $\Sigma_{\rm SFR} \propto \Sigma_{\rm FIR} \propto L_{\rm FIR}^{0.44}$. Empirically, HyLIRGs appear to remain at or below $\Sigma_{\rm SFR} \approx 100\,M_\odot\,{\rm yr^{-1}\,kpc^{-2}}$, with a similar distribution as ULIRGs with luminosities a decade lower (e.g., J. A. Hodge et al. 2019; T. J. L. C. Bakx et al. 2024a; P. S. Kamieneski et al. 2024a), suggesting that $\Sigma_{\rm SFR}$ may even saturate. If this property plays an important role in the K. E. Whitaker et al. (2017) relation, then the obscured fraction may also saturate.

While clearly only a fraction of the star formation is visible in the unobscured mode for these objects, we emphasize that their total SFRs are large enough that the absolute unobscured star formation can still be quite substantial. Moreover, these large color excesses $E(B-V)$ primarily quantify the dust attenuation within the more obscured star-forming regions (e.g., V. Wild et al. 2011; S. H. Price et al. 2014; C.-C. Chen et al. 2020), which D. Calzetti (1997) found differed as $E(B-V)_{\rm stellar} = 0.44\,E(B-V)_{\rm nebular}$. Deviation from this toward greater color excess for the nebular component appears to correlate with specific SFR (sSFR $\equiv {\rm SFR}/M_\star$), since a greater share of star formation occurs in the obscured mode (N. A. Reddy et al. 2015), but it also is likely to vary spatially within individual galaxies (e.g., C. Robertson et al. 2024). It is probably not reasonable to expect that DSFGs will have uniformly large dust attenuation of $A_V \sim$ 4–7, but this remains to be tested more rigorously in larger samples. It is also worth noting that multiband JWST (or even HST) imaging enables robust spatially resolved SED fitting for a wide range of redshifts (e.g., Abdurro'uf et al. 2023; C. Giménez-Arteaga et al. 2023; P. S. Kamieneski et al. 2024b; Z. Liu et al. 2024; M. Polletta et al. 2024; H. B. Akins et al. 2025; T. Harvey et al. 2025), such that the distribution of star formation and dust attenuation can be characterized at subkiloparsec scales. This exercise is crucial to gain an understanding of where SNe might be attenuated beyond detection limits, and even to better model the light curve of any SNe that are detected. This can also help account for any contribution to $L_{\rm IR}$ from dust-obscured AGN in PASSAGES galaxies; K. C. Harrington et al. (2016) and D. A. Berman et al. (2022) use mid- and far-infrared photometry to show that they are star formation-dominated, but not incontrovertibly.

[18] Note the different definition from K. E. Whitaker et al. (2017) for $f_{\rm obsc}$, which also differs in their computation of ${\rm SFR_{IR}}$ using a calibration from UV and 24 μm photometry (K. E. Whitaker et al. 2014).

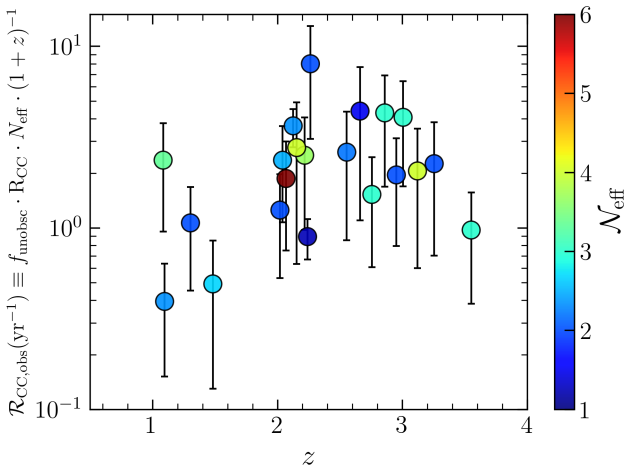

Figure 2. Observable rate of CCSNe $\mathcal{R}_{\rm CC,obs}$ versus redshift for the 21 PASSAGES galaxies considered, using $\mathcal{R}_{\rm CC,obs}$ as defined in Equation (7). The unobscured fractions adopted are provided in Table 1. Colors show the effective multiplicity, $\mathcal{N}_{\rm eff}$, described in Equations (1) and (2). The increase with redshift is predominantly due to a general increase in SFR with z, which is also responsible for the trend observed in Figure 4 (see Section 3.3).

3. Results

3.1. Computing Expected Intrinsic and Observer-frame Rates of CCSNe

Since the progenitors of CCSNe are massive stars, the core-collapse rate is linearly related to the rate of star formation,

$$R_{\rm CC} = k_{\rm CC} \cdot {\rm SFR} \tag{5}$$

(e.g., P. Madau et al. 1998). The factor $k_{\rm CC}$ is determined from the initial mass function (IMF), $\phi(M)$, integrated over the mass range of progenitors, typically 8 $M_\odot$ (S. J. Smartt 2009) to 50 $M_\odot$ (T. Tsujimoto et al. 1997),

$$k_{\rm CC} = \frac{\int_{8\,M_\odot}^{50\,M_\odot} \phi(M)dM}{\int_{0.1\,M_\odot}^{125\,M_\odot} M \cdot \phi(M)dM}, \tag{6}$$

where the denominator is limited to the total mass range of 0.1–125 $M_\odot$. Given that the SFR estimates used in this work are based on a P. Kroupa (2001) IMF, we adopt a value of $k_{\rm CC} = 0.0104\,M_\odot^{-1}$. This is consistent with the optically thick regime ($\epsilon \approx 1$) of Equation (5) of S. Mattila & W. P. S. Meikle (2001), $R_{\rm CC}/{\rm yr^{-1}} = 1.1 \times 10^{-12} \cdot \epsilon^{-1} \cdot L_{\rm FIR}/L_\odot$, where ϵ is the fraction of optical/UV energy absorbed and reradiated in the far-infrared. In comparison, for a E. E. Salpeter (1955) IMF,[19] this yields $k_{\rm CC} = 0.0070\,M_\odot^{-1}$ (e.g., D. R. Young et al. 2008; J. Melinder et al. 2012).

In Figure 2, we show the observable rate of CCSN images[20]

$$\mathcal{R}_{\rm CC,obs} \equiv f_{\rm unobsc} \cdot R_{\rm CC} \cdot \mathcal{N}_{\rm eff} \cdot (1+z)^{-1} \tag{7}$$

against redshift, with intrinsic rate $R_{\rm CC}$ determined from the intrinsic (i.e., magnification-corrected) ${\rm SFR_{IR}}$. The apparent

[19] For completeness, a G. Chabrier (2003) IMF integrated over the same progenitor mass ranges gives $k_{\rm CC} = 0.0110\,M_\odot^{-1}$, closer to that for the Kroupa IMF. However, since converting from a Salpeter to Chabrier IMF also lowers the SFR by a factor of 0.63 (P. Madau & M. Dickinson 2014), the resulting $R_{\rm CC} = 0.0069 \cdot {\rm SFR_{Salpeter}}$, thus certainly consistent within uncertainties.

[20] To minimize confusion, we use $\mathcal{R}$ when referring to what we define as the observable rate, and simply R when referring to an intrinsic, rest-frame rate.

rates, μSFR, and magnifications μ are retrieved from the references given in Table 1. Given the dusty nature of these sources, we include $f_{\rm unobsc}$ in the equation ab initio, for a more realistic quantification of expected rates. This does not quantify the fraction of SNe that could be detectable in any observational campaign but is more akin to a maximum recoverable fraction for what is reasonable with current telescope facilities. For comparison, I. Mäntynen et al. (2025) recently found that the undetectable fraction of CCSNe in low-z LIRGs for a survey sensitive to $A_V < 16$ mag is $66^{+8.6}_{-14.6}\%$. Using our formulation, this would suggest $f_{\rm unobsc} = 34^{+14.6}_{-8.6}\%$. For a much shallower survey down to $A_V < 3$ mag, they found instead an undetectable fraction of $89.7^{+2.6}_{-4.4}\%$.

The large uncertainties in $\mathcal{R}_{\rm CC,obs}$ are the direct result of a combination of (i) the broad range chosen for $f_{\rm unobsc}$, (ii) inherently large uncertainty in $\rm SFR_{IR}$, (iii) large uncertainty in magnification μ for the current lens models, and (iv) the conservative fractional uncertainties used for the effective multiplicity $\mathcal{N}_{\rm eff}$. However, despite this uncertainty, the median $\mathcal{R}_{\rm CC,obs}$ is very high at $\sim$2 $\rm yr^{-1}$, especially considering the average volumetric rates of $\sim 10^{-4}$–10^{-3} $\rm yr^{-1}\,Mpc^{-3}$ at Cosmic Noon (T. Dahlen et al. 2012; L.-G. Strolger et al. 2015). As discussed in Section 2.4, the infrared-inferred SFRs are likely the closest to the true SFRs for these dust-obscured galaxies, but they are not necessarily representative of the rates of SNe that one could expect to observe. We adopt a typical value of $f_{\rm unobsc} = 0.2 \pm 0.1$, following the findings of Balmer decrements for two members of the sample and for other DSFGs in the literature (Section 2.4).[21]

In Section 3.3, we compare the predicted rates $R_{\rm CC}$ (and the rate of SNe Ia) for PASSAGES with those from other works that also examine candidate samples for SN monitoring, alongside the expected rates for host galaxies of some of the already discovered glSNe. In Figure 2, we observe an increase in $\mathcal{R}_{\rm CC,obs}$ with redshift, which is likely to be driven primarily by the generally higher SFRs in the sample above $z \gtrsim 2$ (whereas $\mathcal{N}_{\rm eff}$ is essentially constant with redshift). In Section 3.3, we discuss how this compares with the redshift evolution of the cosmic SFR density.

3.2. Estimating the Rate of SNe Ia

Since the progenitors of SNe Ia are best understood to be binary systems that include a white dwarf star, the rate of SNe Ia inherently depends in part on the number of evolved lower-mass stars (A. J. Ruiter & I. R. Seitenzahl 2025). In turn, since these make up the bulk of the stellar mass of a typical galaxy, it is reasonable to expect that the rate of SNe Ia $R_{\rm Ia}$ would increase with $M_\star$ (either linearly or with some positive power law). The donor star from which the progenitor white dwarf accretes may itself be another white dwarf or a main-sequence or giant star, which implies that $R_{\rm Ia}$ should also have some dependence on the SFR, as with $R_{\rm CC}$.

F. Mannucci et al. (2005) and E. Scannapieco & L. Bildsten (2005) found that the observed rate of SNe Ia could be described as a two-component linear combination of SFR and $M_\star$ (see also M. Sullivan et al. 2006). M. Smith et al. (2012) included a power law for both terms in their bivariate parameterization, favoring

$$\begin{aligned} R_{\rm Ia} &= (1.05 \pm 0.16) \times 10^{-10}\, M_\star{}^{0.68\pm0.01} \\ &\quad + (1.01 \pm 0.09) \times 10^{-3}\, \rm SFR^{1.00\pm0.05} \\ &\approx (6.6 \pm 1.0) \times 10^{-4} \left(\frac{M_\star}{10^{10}\,M_\odot}\right)^{0.68\pm0.01} \\ &\quad + (1.0 \pm 0.1) \times 10^{-1} \left(\frac{\rm SFR}{100\,M_\odot\ \rm yr^{-1}}\right)^{1.00\pm0.05} \end{aligned} \tag{8}$$

with a "prompt" term and a "delayed" term (although this is for a sample at $z < 0.25$). M. Sullivan et al. (2006) found that the rate of SNe Ia per unit mass increases with increasing sSFR, which may partly explain the sublinear dependence on $M_\star$. A more rigorous treatment would use the star formation history (SFH) convolved with the delay time distribution (DTD; P. Madau et al. 1998; F. Mannucci et al. 2006). Instead, the "A+B" parameterization with $M_\star$ and SFR essentially samples the continuous SFH and DTD at two times (D. Maoz et al. 2014). However, as cautioned by P. Andersen & J. Hjorth (2018), this calibration is unconstrained for starburst galaxies with $\log(sSFR) > -9$. While this dependency may in principle also evolve with redshift, several combinations of cosmic star formation histories and DTDs tested by P. A. Palicio et al. (2024) were able to adequately fit the observed rates of SNe Ia (which are themselves still quite uncertain above $z > 2$). For our purposes, we consider it justifiable to use M. Smith et al.'s (2012) results—derived from a wide range of $8 < \log(M_\star/M_\odot) < 11$—to make predictions for our sample.

Unfortunately, the stellar masses for the majority of the PASSAGES DSFGs remain unconstrained, but they are at least very likely to be on the massive end of the stellar mass function ($\log(M_\star/M_\odot) > 10.5$) given their extreme luminosities and molecular gas masses (K. C. Harrington et al. 2021). While most are actually detected in H-band imaging with HST (P. S. Kamieneski et al. 2024a), insufficient observed-frame near-infrared data have been collected so far to enable robust SED fitting for most of the background lensed sources,[22] apart from two exceptions. For the pair of interacting DSFGs behind the G165 cluster, JWST NIRCam and NIRSpec observations yield stellar masses of $\log_{10} M_\star \approx 10.2$ and 10.3 (B. L. Frye et al. 2024; P. S. Kamieneski et al. 2024b). With their infrared-inferred SFRs, their sSFRs are both 0.9 dex above the MS, but the likely tidal interaction between the two galaxies might be driving an elevated starburst phase above the rest of the sample. In addition, D. Liu et al. (2024) found a large stellar mass of $\log(M_\star/M_\odot) \approx 11.2 \pm 0.4$ for PJ0116-24 with $\rm SFR_{IR} \approx 1480\,M_\odot\,yr^{-1}$, which is 0.8 dex above the star-forming main sequence (SFMS).

In Appendix A, we use the expected offset of DSFGs from the SFMS to gain an imprecise estimate of reasonable stellar masses. However, ultimately the dependence of Equation (8) on $M_\star$ is highly subdominant to the contribution from SFR in the star-forming regime ($\rm SFR \gtrsim 10\,M_\odot\,yr^{-1}$). Fortunately, this allows us to still predict $R_{\rm Ia}$ for the sample within reason,

[21] As noted in Table 1, for two exceptions we use the direct measurements of $f_{\rm unobsc}$ that are available for PJ0116-24 (D. Liu et al. 2024) and PJ1127+42 (B. L. Frye et al. 2024).

[22] In principle, lensing-corrected rest-frame K-band luminosity may correlate with stellar mass (e.g., T. H. Jarrett et al. 2013) and could be determined for $z \sim 2$ with WISE at 4.6 μm, for example. However, there is likely significant differential magnification between the stellar continuum and dust continuum, and measuring the magnification factors for the rest-frame near-infrared is beyond the scope of this work.

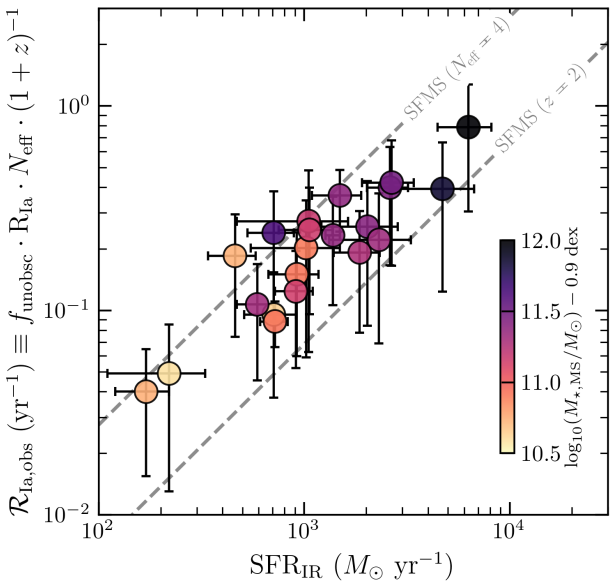

Figure 3. For the same galaxies as in Figure 2: predicted observer-frame rates $\mathcal{R}_{\rm Ia,obs}$ of SNe Ia (the intrinsic rate $R_{\rm Ia}$ multiplied by the unobscured fraction $f_{\rm unobsc}$, the effective number of multiple images $\mathcal{N}_{\rm eff}$ and the time dilation factor, $(1+z)^{-1}$). In this regime of active star formation, $R_{\rm Ia}$ is primarily a function of SFR and weakly dependent on $M_\star$. Stellar masses are bounded by assuming that the sSFRs lie between 0.3 dex below and 0.9 dex above the SFMS. Colors of data points show this effective lower limit on $M_\star$ for 0.9 dex above the SFMS. A dashed gray line shows the expected rate for a galaxy exactly on the SFMS at $z = 2$ according to the J. S. Speagle et al. (2014) treatment, and a second dashed line shows the observable rate for the same galaxy with an effective multiplicity of $\mathcal{N}_{\rm eff} = 4$.

which we include in Table 1. In Figure 3, we show the predicted observable rates of SNe Ia for PASSAGES, $\mathcal{R}_{\rm Ia,obs} \equiv f_{\rm unobsc} \cdot R_{\rm Ia} \cdot \mathcal{N}_{\rm eff} \cdot (1+z)^{-1}$, as a function of their SFR$_{\rm IR}$. In this regime of star formation, the SN Ia rates are dominated by the contribution from SFR, but the data points' colors correspond to the lower limits in stellar masses that we adopt, at 0.9 dex above the SFMS. In Figure 4, we show the observable rates $\mathcal{R}_{\rm Ia,obs} \cdot (f_{\rm unobsc})^{-1}$ versus redshift,[23] with transparent points indicating the intrinsic rates $R_{\rm Ia}$. This particularly emphasizes our finding that the decrement in observable rate due to redshift time dilation is approximately counteracted by the boost provided by multiple imaging.

3.3. Predicting the Rate of Independent Supernova Events

Up to this point, we have considered the rate of observable SNe from Earth's perspective, taking into account both cosmological time dilation by $(1+z)^{-1}$ and amplification by multiple imaging $\mathcal{N}_{\rm eff}$. This rate is useful if one's goal is to catch any image of a glSN, but if the goal is to perform TD cosmography, then the rate of independent SNe events is of greater interest.[24] We show these rates for PASSAGES in Figure 5, along with the predicted rates from similar works forecasting glSN rates in targeted monitoring searches,

[23] Dividing $\mathcal{R}_{\rm Ia,obs}$ by the obscured fraction in this version reduces the relative uncertainties and thus makes it easier to interpret. Given that $R_{\rm Ia}$ is dominated by the SFR, we expect the SNe Ia to be subject to roughly the same average attenuation as the CCSNe, but few works have yet examined this at these redshifts.

[24] Here, this rate still accounts for $R_{\rm CC}$ and $R_{\rm Ia}$ being modulated by $(1+z)^{-1}$ time dilation but not by $f_{\rm unobsc}$ to allow for a more direct comparison with values in the literature.

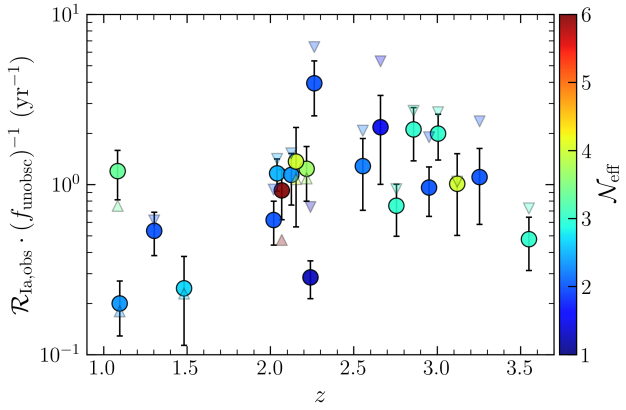

Figure 4. Redshift distribution of the observable rate of SNe Ia from PASSAGES estimated in Figure 3, $\mathcal{R}_{\rm Ia}$, but now removing the factor of $f_{\rm unobsc}$ (thus reducing uncertainties and improving legibility). Colors indicate the effective multiplicity $\mathcal{N}_{\rm eff}$. Transparent, smaller triangles indicate the intrinsic rates ($R_{\rm Ia}$) for each target (i.e., without factoring in the boost from multiple imaging or the $1+z$ decrement from cosmological time dilation). The triangles for intrinsic rates are oriented to point toward their corresponding observable rates. This illustrates that since $\mathcal{N}_{\rm eff} \cdot (1+z)^{-1}$ is typically of order unity, these effects roughly cancel out.

including the Frontier Fields (T. Petrushevska et al. 2018a, 2018b) and 128 galaxy-scale lenses from Y. Shu et al. (2018, 2021). We also indicate rates from the host galaxies of a number of the already discovered glSNe—e.g., the CCSN Refsdal (P. L. Kelly et al. 2015) in a galaxy lensed by MACS J1149, and the set of SNe Ia that includes SN Requiem/SN Encore (S. A. Rodney et al. 2021; J. D. R. Pierel et al. 2024b) in MRG-M0138 (A. B. Newman et al. 2018) and SN H0pe in G165 Arc 2abc (B. L. Frye et al. 2024).

While $R_{\rm CC}$ and $R_{\rm Ia}$ might appear at first to be equivalent to within a constant factor, this is not quite the case. By Equations (5) and (8), the ratio $R_{\rm Ia}/R_{\rm CC} \sim {\rm sSFR}^{-1} \cdot M_\star^{-0.32}$ (plus a constant term). By the SFMS, many of the star-forming galaxies included in Figure 5 will have comparable values of sSFR, while the ratio is more weakly dependent on $M_\star$. For a $10^{10}\,M_\odot$ galaxy on the main sequence at $z \sim 2$, for example, $R_{\rm Ia}/R_{\rm CC} \approx 0.1$ (adopting a Kroupa IMF).

Every PASSAGES object included in this work exceeds the rate of all other targets considered in Figure 5, demonstrating the dramatic potential of this sample. Most are even >2 dex above typical arcs in the Frontier Fields; while these clusters are remarkable for their lensing power, the background objects are largely unremarkable in terms of their SFR. Perhaps more surprising is the observation that our predictions for $R_{\rm CC}$ are all $\gtrsim$1.5 dex above the host galaxy of S. Refsdal, and even our predicted $R_{\rm Ia}$ are $\gtrsim$1 dex above MRG-M0138, the host of two recent SNe Ia, Requiem and Encore. We also observe that the redshift-dilated $R_{\rm CC}$ and $R_{\rm Ia}$ rates for PASSAGES roughly increase with redshift (likely owing to their identification by flux; see Figure 2 of Q. D. Wang et al. 2024). This trend is contrary to the slow decline of the (dilated) cosmic SFR density, $\psi(z) \cdot (1+z)^{-1}$ (P. Madau & M. Dickinson 2014), shown as a gray curve in Figure 5.

In absolute terms, the median (Earth-frame) occurrence rate of individual CCSNe is 3.5 yr^{-1} and $\sim$0.3 yr^{-1} for SNe Ia. This does not imply, we caution, that any 1 year monitoring program would yield multiple glSNe per field, since the actual yield is the occurrence rate multiplied by the control time (F. Zwicky 1938). This is effectively the cumulative

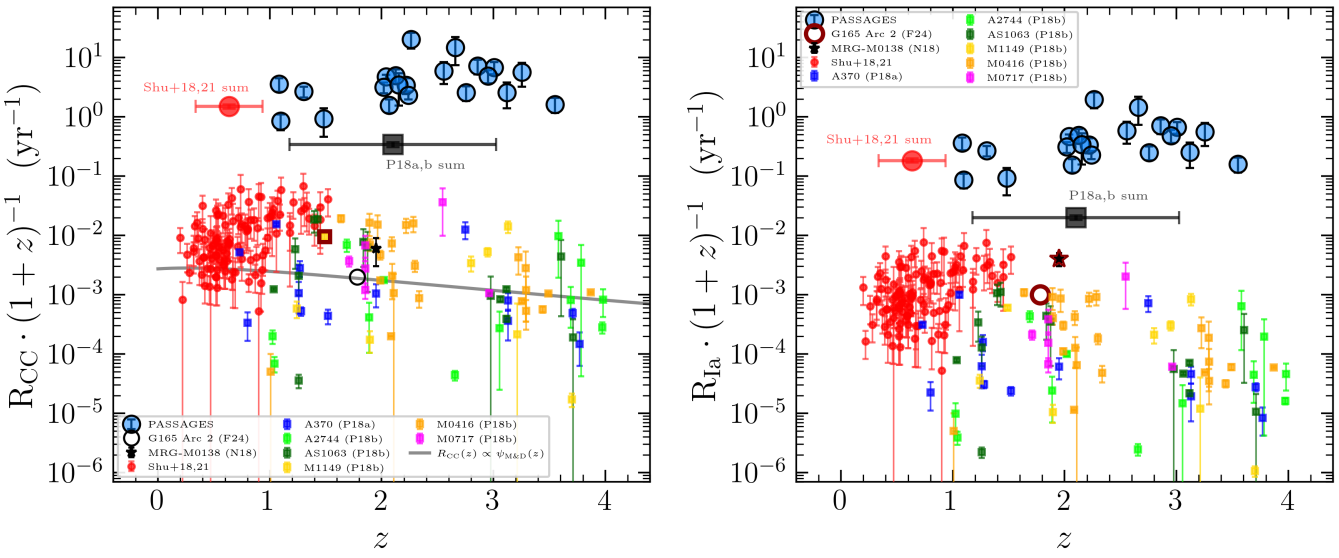

Figure 5. Intrinsic SN rates (CCSNe on left, SNe Ia on right) rescaled by time dilation but excluding multiple imaging (and $f_{\rm unobsc.}$ correction), versus redshift. Whereas $\mathcal{R}_{\rm CC,obs}$ and $\mathcal{R}_{\rm Ia,obs}$ represented the average rate at which SN images appear, $R_{\rm CC} \cdot (1+z)^{-1}$ and $R_{\rm Ia} \cdot (1+z)^{-1}$ are the actual rate of individual SN events, as if the galaxies were not lensed. We compare with the predictions made for a large sample of galaxy–galaxy lenses by Y. Shu et al. (2018), incorporating the corrections from Y. Shu et al. (2021), and the Frontier Fields considered by T. Petrushevska et al. (2018a, 2018b). The sums of the Y. Shu et al. and T. Petrushevska et al. samples are shown as large red circles and large black squares, respectively. Predicted rates for G165 Arc 2, the host galaxy of the Type Ia SN H0pe, are shown with open circles (based on SFR/$M_\star$ from B. L. Frye et al. 2024). Similarly, the predicted rates for MRG-M0138 (based on A. B. Newman et al. 2018) are indicated as black stars (with a dark red border on the right panel, highlighting SN Requiem/Encore). In the left panel, the MACS J1149 point with a dark red border is the host galaxy of the discovered CCSN glSN Refsdal. The PASSAGES objects considered in this work have CCSN rates about 100 times greater than the Y. Shu et al. sample (and similarly for SNe Ia). In the left panel, the gray curve shows the expectation of $R_{\rm CC}(z) \propto \psi(z)$ for the P. Madau & M. Dickinson (2014) parameterization of the cosmic SFR density $\psi(z)$, which has units of $M_\odot$ yr^{-1} Mpc^{-3}, rescaled arbitrarily to approximately match the Frontier Fields data points.

duration for which a given SN would fall above the detection threshold, which itself depends on a combination of observing sensitivity, dust attenuation, lensing magnification, and the precise SN type. We do not simulate a mock observing campaign in this work but simply remark that this sample has $\gtrsim$18 members with core-collapse occurrence rates $R_{\rm CC} \cdot (1+z)^{-1}$ in excess of 1 yr^{-1} (with a median closer to 4 yr^{-1}). As a conservative example, an observer-frame control time of 1 month per epoch, with three epochs over the course of a year, would result in a yield of $N_{\rm CC} \sim 0.5$ detections for each field. If these 18 fields were all monitored at this rate, one could expect to detect ∼9 CCSNe with this campaign alone (not to mention any SNe Ia that are uncovered). With the depths of 28–29 mag routinely reachable by JWST at ∼1.5 μm in ∼1 hr, it is highly feasible to extend the per-epoch control time well beyond 1 month (e.g., Figure 12 of T. Petrushevska et al. 2016), even for only modestly magnified arcs, such that even a subsample would be expected to result in at least one detection.

As another example, we consider SNe Ia, which of course are more uniform in their light-curve behavior and which are themselves predicted to be quite frequent in HyLIRGs. With SN H0pe as a recent example of a $z \sim 2$ glSN Ia in a relatively dusty environment, we note that its demagnified peak was observed at ∼24 mag in F150W (rest-frame V band), but it also remained above 25 mag for a duration of ≈90 days in the observed frame (J. D. R. Pierel et al. 2024a). The light-curve model suggested $A_V = 1.21 \pm 0.11$ (also W. Chen et al. 2024); if the SN were subjected to substantially higher attenuation as might be expected for HyLIRGs, such as $A_V = 5$, then the peak would be ∼4 mag fainter (i.e., ∼28 mag) and the SN would remain above 29 mag for an observer for ∼3 months. With only modest magnification $\mu = 5$ (or 1.7 mag), a 5σ point-source limiting depth of 27.3 mag would be required for a detection, achieved in less than 10 minutes of integration with JWST/NIRCam[25] or <2 orbits with HST WFC3/IR in F160W.

As a caveat, however, the occurrence rates we estimate do not account for the possibility that some detected SN events might be caught only when the last image is still visible. In this hypothetical scenario, there is unlikely to be any hope for performing TD cosmography, since no delays can actually be measured through light curves. It is rather nontrivial to quantify the likelihood of this actually occurring because it depends on both the time delays between images and the control time (such that the penultimate image to arrive has faded below the detection limit but not the final image).

To place these forecasts in context, we compare with the yields that are currently expected from other search strategies. A. Sainz de Murieta et al. (2024) predicted that LSST will uncover ∼7 Type Ia glSNe per year within known galaxy-lensed objects that are suitable for TD cosmography. In this case, the authors note that an H_0 measurement is not feasible if the host galaxy is not itself lensed as well (thereby enabling precise lens modeling). Similarly, N. Arendse et al. (2024) predict a "gold sample" of ∼10 glSNe Ia yr^{-1} uncovered with LSST that are sufficiently bright and with time delays that are long enough to enable follow-up observations (which are likely essential; S. Huber et al. 2019). Complementary to this will be an approach of monitoring a "watchlist" of lensing galaxy clusters (D. Ryczanowski et al. 2023), which are beneficial for reasons discussed in Section 3.4. M. Bronikowski et al. (2025) predict one to two such SNe will be discovered by LSST per

[25] Sensitivity is estimated with the JWST Exposure Time Calculator (K. M. Pontoppidan et al. 2016).

year from a sample of 46 well-studied lensing clusters. The SNe Ia cosmology program of the upcoming Nancy Grace Roman Space Telescope (R. Hounsell et al. 2018) will also reveal some fraction that are gravitationally lensed (M. Oguri & P. J. Marshall 2010), which may number as high as ∼11 glSNe Ia and ∼20 cumulative lensed CCSNe (J. D. R. Pierel et al. 2021).

3.4. Identifying Candidates with the Longest Median Time Delay

Cluster-scale lenses are typically the best candidates for high rates of lensed SNe in the observed frame due to their large lensing cross sections $\sigma(z_s)$ in the source plane at z_s (E. L. Turner et al. 1984). This cross section is closely linked to the Einstein radius

$$\theta_E = \left[\frac{4GM(<\theta_E)}{c^2} \cdot \frac{D_{LS}}{D_L D_S} \right]^{1/2} \quad (9)$$

(e.g., R. Narayan & M. Bartelmann 1996) for enclosed mass $M(<\theta_E)$ and angular-diameter distances to the lens (D_L), to the source plane (D_S), and between these two (D_{LS}). To first order, the area that produces four lensed images from a singular isothermal ellipsoid (again excluding demagnified images) is $\sigma_4 = \pi\epsilon^2\theta_E^2/6$ (P. Schneider al. 2006), where $\epsilon \equiv 1 - b/a$ is the ellipticity (from major and minor axes, a and b). The cross section then scales linearly with mass, $\sigma_4 \propto M(<\theta_E)$, such that a cluster can have orders of magnitude larger areas. As discussed in Section 2.2, this larger area of magnification means that a galaxy is more likely to be lensed uniformly into a constant multiplicity of images, but it also means that objects nearby in projected distance will also be multiply imaged (Section 3.6). This further amplifies the expected rate of observable SNe.

Cluster lenses with large Einstein radii are also beneficial for following up lensed SNe for the purpose of TD cosmography (e.g., M. Bronikowski et al. 2025). It is true that time delays between any pair of cluster-lensed images can still be very short (e.g., a few days)—especially in the case where the deflection is dominated by a galaxy- or group-scale halo embedded within the cluster. For example, this was the case with the first four images of S. Refsdal, which formed an Einstein cross configuration ($\theta_{\rm Ein} \approx 1.3$; delays ≈10–20 days; P. L. Kelly et al. 2023a) around an elliptical galaxy in the cluster at $z = 0.54$ (P. L. Kelly et al. 2015). However, one should expect that a larger Einstein radius (or angular separation between images) would correlate with a larger median delay, by virtue of the longer path lengths followed by the highly deflected light rays.

In practice, varying approaches are used to quantify the Einstein radius of a system (see for example Section 3.5 of P. S. Kamieneski et al. 2024a). For the PASSAGES objects in this work, the values of $\theta_{\rm Ein}$ shown in Table 2 are derived according to the equivalent Einstein radius definition, which is the radius of the smallest circle centered on the peak of lensing convergence κ that contains an average $\langle\kappa\rangle < 1$ (P. Schneider et al. 1992). For lensed systems with multimodal mass distributions, different Einstein radii may be measured for the different mass components. This notably includes G165, the field containing both SN H0pe and the PJ1127+42 DSFG. With the model from P. S. Kamieneski et al. (2024b), we measure $\theta_{\rm Ein} = 10\farcs7 \pm 1\farcs1$ for the $z = 2.24$ DSFG arc on the southwest side of the cluster, and $21\farcs1 \pm 0\farcs5$ for the $z = 1.78$ arc hosting SN H0pe on the northeast side. B. L. Frye et al. (2019) measured a lens size of 13″, but with a different definition (based on the total area inside the critical curve for the full cluster). M. Pascale et al. (2022) measured 15.″3 for $z = 9$ using the same approach, or ≈14.″4 rescaled to $z_s = 2.24$, although this and the B. L. Frye et al. measurement were made before new constraints from NIRCam were available (B. L. Frye et al. 2024).

For other previously discovered glSNe summarized at the bottom of Table 2, the Einstein radii are estimated using the publicly available Frontier Fields lens models (J. M. Lotz et al. 2017). For these, we also employ a model-independent approach to determine the radius of a circle that best captures the distribution of features/clumps within the lensed arcs (e.g., J. D. Remolina González et al. 2020; S. D. Mork et al. 2025).

Figure 6 shows the median lens model-predicted time delay ($\widetilde{t_d}$) versus Einstein radius for the PASSAGES sample, along with the observed/predicted values for the set of known glSNe. The time delays are estimated for the position of the approximate centroid of each arc (or the location of corresponding counter-images, if this differs substantially). These time delays will have large uncertainties, in part because the delays that would actually be observed depend strongly on the actual position of any glSNe. The median $\widetilde{t_d}$ will still have large uncertainty, given that most arc families have only two to four images, but is sufficient for our purpose of looking for a trend with $\theta_{\rm Ein}$. While there is a decent amount of scatter—especially at the high-θ_E, high-t_d end—there is a clear strong correlation between t_d and θ_E (Spearman's rank correlation coefficient $\rho = 0.89$, with high significance $p \ll 0.01$), such that θ_E may be used to select likely long-delay lenses as a rule-of-thumb. As we discuss in Appendix B, this correlation has some theoretical underpinning, since time delays can be related to the image separations of arcs relative to the lens centroid.

3.5. Optimizing the Success of a Random Monitoring Program

Ideally, for a monitoring program to be successful, time delays between images should be relatively comparable to the average duration between SNe in the observer-frame—i.e., $\tau_{\rm SN} \equiv (R_{\rm CC} + R_{\rm Ia})^{-1} \cdot (1 + z)$. If the median time delay is much less than this characteristic time between SNe, $\widetilde{t_d} \ll \tau_{\rm SN}$, then multiple imaging does not contribute very favorably to boosting the rate of observable SNe. In this scenario, there would still be long durations where no SN images would be visible, presenting challenges for monitoring campaigns. The PASSAGES targets and the hosts of some of the confirmed glSNe in the literature are shown in Figure 7. There are also unique challenges for fields with very short $\tau_{\rm SN}$ timescales (e.g., less than 1 month observed frame) because it can then become difficult to confirm that transient events seen in multiple images of a galaxy are in fact images of the same SN. This risk of confusion can certainly be mitigated: information on parity and relative location of the transient within the arc can be helpful in ruling out unrelated events. Very few targets are likely to lie in this regime and a well-refined lens model can assist in assessing the reliability of glSN candidates. For PASSAGES, for example, PJ0846+15 nominally has a very short $\tau_{\rm SN}$, but in reality the very high SN rates arise from a very high SFR from multiple galaxies in a candidate protocluster

Table 2
Einstein Radii and Median Time Delays Estimated from the Lens Model for PASSAGES Targets and for GlSNe Drawn from the Literature

ID	z_l	z_s	$\theta_{\rm Ein}$ (arcsec)	$\widetilde{t}_d$[a] (days)	max t_d[a] (days)	References[b]
PJ0116−24	0.555	2.125	2.37 ± 0.04	72	201	(1)
PJ0143−01	0.594	1.096	0.53 ± 0.08	3.4	10	(1)
PJ0209+00	0.202	2.554	2.6 ± 0.2	56	60	(1)
PJ0226+23	0.41	3.120	3.6 ± 0.3	110	190	(1)
PJ0305−30	0.5	2.263	0.6 ± 0.1	11	11	(1)
PJ0748+59	0.402	2.755	16.2 ± 1.3	3600	5400	(2, 3)
PJ0846+15	0.766	2.664	5.5 ± 1.6[c]	560[c]	780[c]	(4)
PJ1053+60	0.837	3.549	5.9	…	…	(5)
PJ1053+05	1.525	3.005	0.71 ± 0.04	23	62	(1)
PJ1127+46	0.42	1.303	0.58 ± 0.06	14	14	(1)
PJ1127+42	0.348	2.236	10.7 ± 1.1	470	580	(6, 7)
PJ1138+32	0.52	2.019	0.40 ± 0.05	14	16	(1)
PJ1139+20	0.57	2.858	0.7 ± 0.4	46	59	(1)
PJ1322+09	0.6	2.068	6.1 ± 1.0	420	560	(3)
PJ1326+33	0.786	2.951	1.8 ± 0.2	510	580	(1)
PJ1329+22	0.44	2.040	11.0 ± 0.4	…	…	(8)
PJ1336+49	0.26	3.254	1.2 ± 0.1	36	39	(1)
PJ1446+17	0.493	1.084	0.82 ± 0.05	12	14	(1)
PJ1449+22	0.4	2.153	6.5 ± 1.2	300	460	(1)
PJ1607+73	0.65	1.482	1.0 ± 0.1	35	36	(1)
PJ2313+01	0.560	2.217	2.1 ± 0.2	58	94	(1)
Literature						
PS1-10afx	1.117	1.388	0.12	1.3	…	(9, 10)
S. Refsdal(S1-S4)	0.54	1.49	1.37 ± 0.08[b]	4	…	(11, 12)
S. Refsdal(SX)	…	…	4.5[b]	380	…	(11, 13)
iPTF16geu	0.216	0.409	0.3	1.4	…	(14, 15, 16)
SN Requiem/Encore	0.338	1.95	18.8 ± 1.1	7800	…	(17, 18, 19)
SN Zwicky	0.226	0.354	0.168	0.42	…	(20, 21)
SN A370-C22	0.375	2.93	1.0 ± 0.5[b]	31	…	(22)
SN H0pe	0.348	1.78	21.1 ± 0.5[b]	83	…	(6, 23)

Notes.
[a] Median (and maximum) time delays for PASSAGES objects derived in this work (unless otherwise noted) using lens models from the supplied references. The representative values are simply determined by taking the median/maximum of the delays from the first image in each lensed system to arrive. Estimates are not currently available for PJ1053+60 and PJ1329+22.
[b] References for table values, roughly in order of columns (e.g., SN discovery if applicable, followed by redshifts, then $\theta_{\rm Ein}$, and finally time delays). For SN Requiem/Encore, $\theta_{\rm Ein}$ is determined by rescaling $\theta_{\rm Ein}(z \to \infty)$ from S. Ertl et al. (2025) to $z_s = 1.95$.
[c] Estimated in this work. The Einstein radii for the SNe in A370 and MACS J1149 (Refsdal) are taken as the median $\theta_{\rm Ein}$ derived from the publicly available convergence maps from the Frontier Fields (J. M. Lotz et al. 2017) lens models at https://archive.stsci.edu/prepds/frontier/lensmodels —in particular, the CATS, GLAFIC, and Sharon models (given their similarity to the LENSTOOL models used for the PASSAGES objects). The range of values are combined with our own empirical measurements according to the method from S. D. Mork et al. (2025). For PJ0846+15, $\theta_{\rm Ein}$ and $\widetilde{t}_d$ are estimated for the Einstein cross system, 12abcd (N. Foo et al. 2025).
References: (1) P. S. Kamieneski et al. 2024a; (2) S. Amodeo et al. 2018; (3) P. Kamieneski et al. 2026, in preparation; (4) N. Foo et al. 2025; (5) Q. D. Wang et al. 2024; (6) B. L. Frye et al. 2024; (7) P. S. Kamieneski et al. 2024b; (8) A. Díaz-Sánchez et al. 2017; (9) R. Chornock et al. 2013; (10) R. M. Quimby et al. 2014; (11) P. L. Kelly et al. 2015; (12) S. A. Rodney et al. 2016; (13) P. L. Kelly et al. 2023b; (14) A. Goobar et al. 2017; (15) J. M. Diego et al. 2022; (16) S. Dhawan et al. 2020; (17) S. A. Rodney et al. 2021; (18) J. D. R. Pierel et al. 2024b; (19) S. Ertl et al. 2025; (20) A. A. Goobar et al. 2022; (21) J. D. R. Pierel et al. 2023; (22) W. Chen et al. 2022; (23) J. D. R. Pierel et al. 2024a.

core (N. Foo et al. 2025), in which case it is much easier to rule out unrelated transient events.

The sample members with the longest predicted median time delays >100 days include (in descending order) PJ0748+59, PJ0846+15, PJ1326+33, PJ1127+42, PJ1322+09, PJ1449+22, and PJ0226+23. These are also among the widest-separation targets, as expected, despite the large uncertainties in $\widetilde{t}_d$. Except for PJ0226+23, these all also have $\widetilde{t}_d > \tau_{\rm SN}$ and $\mathcal{R}_{\rm CC,obs} + \mathcal{R}_{\rm Ia,obs} > 1$. This upper echelon only considers the $\mathcal{R}$ rates and expected time delays—i.e., not magnification, dust attenuation, or other factors that influence the control time.

Finally, we note that the vast majority (90%) of objects in the full sample have an expected value of multiplicity, $\mathcal{N}_{\rm eff} > 2$. This suggests that SNe hosted by the primary DSFGs in these fields are likely to be multiply imaged (and not just weakly lensed into a single image), and therefore hypothetically suitable for time-delay analyses—although $\mathcal{N}_{\rm eff} < 2$ certainly does not mean glSNe are not possible. In the next section, we discuss contribution from other galaxies in the fields nearby to the DSFGs that might also be lensed into multiple images, but this generally requires a large lensing cross section that can only be attributed to galaxy cluster lenses.

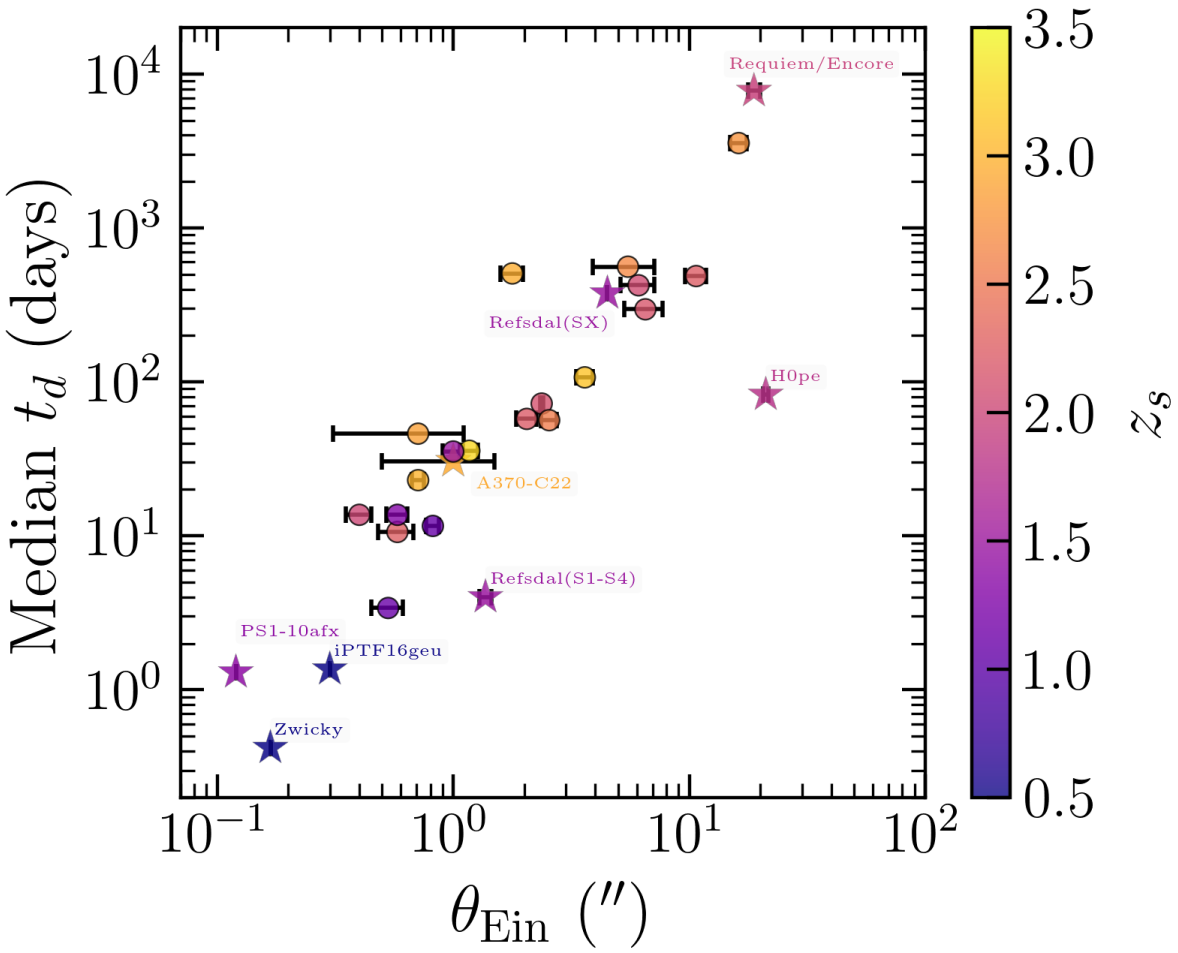

Figure 6. Median time delays t_d (between the first image to arrive and the other multiple images) in days versus the Einstein radius θ_E in arcsec; see Table 2. Lensed SNe from the literature (and their time delay/Einstein radius measurements) shown as stars include PSF1-10afx (R. Chornock et al. 2013; R. M. Quimby et al. 2013, 2014), S. Refsdal (for both the Einstein Cross images S1-S4 and the last image SX; P. L. Kelly et al. 2015, 2016, 2023b; S. A. Rodney et al. 2016), iPTF16geu (A. Goobar et al. 2017; J. M. Diego et al. 2022), SN Requiem (S. A. Rodney et al. 2021), SN Zwicky (A. A. Goobar et al. 2022; A. Goobar et al. 2023; J. D. R. Pierel et al. 2023), the $z = 2.9$ SN discovered by W. Chen et al. (2022), and SN H0pe (B. L. Frye et al. 2024; J. D. R. Pierel et al. 2024a); see review by S. H. Suyu et al. (2024). For SN H0pe and the SX image of S. Refsdal, the time delays are the values derived from the photometric light curve; in all other cases, delays are lens model predicted. Despite the scatter, there is a statistically significant correlation between $\widetilde{t_d}$ and θ_E, validating the assumption that larger image separations generally yield longer time delays (see Appendix B).

3.6. Contribution from Galaxy-overdense Regions

Thus far, our estimated SN rates have been limited to the lensed DSFGs that were responsible for the submillimeter flux by which the PASSAGES sample was selected. However, this does not account for the contributions from other galaxies that might also be gravitationally lensed, especially in the case of cluster-scale lenses with wide caustic networks. Numerous recent works have revealed that DSFGs, like other very massive galaxies (T. R. Greve et al. 2005), might be effective signposts of protoclusters (or at least overdense regions; G. Kauffmann et al. 1999; Y.-K. Chiang et al. 2013; reviews by R. A. Overzier 2016; S. Alberts & A. Noble 2022). This complements the established association of protoclusters with overdensities of Hα and Lyα emitters, High-z Radio Galaxies, and Lyman Break Galaxies (e.g., C. De Breuck et al. 2004; B. P. Venemans et al. 2007; G. Miley & C. De Breuck 2008; E. Daddi et al. 2009; P. L. Capak et al. 2011; A. B. Drake et al. 2020). R. C. Hickox et al. (2012) and S. M. Stach et al. (2021) found that DSFGs are more strongly clustered than typical star-forming galaxies at comparable redshifts, with autocorrelation lengths consistent with those of quasars (A. D. Myers et al. 2009). The rich set of literature with evidence for DSFGs (or overdensities of DSFGs) as protocluster signposts includes D. A. Riechers et al. (2010), H. Dannerbauer et al. (2014), C. M. Casey et al. (2015), H. Umehata et al. (2015), C. M. Casey (2016), D. L. Clements et al. (2016), C.-L. Hung et al. (2016), V. Smolčić et al. (2017), A. J. R. Lewis et al. (2018), T. B. Miller et al. (2018), R. Pavesi et al. (2018), and R. Calvi et al. (2023). Two members of the PASSAGES sample have themselves been highlighted as protocluster candidates (B. L. Frye et al. 2024; N. Foo et al. 2025). On the other hand, DSFGs may not be efficient tracers of overdensities at all redshifts. T. B. Miller et al. (2015) suggest that since $z \lesssim 2.5$, the high-mass end of galaxies within the most massive dark matter halos have already quenched their star formation and ceased to be submillimeter bright.

Semianalytic modeling by P. Araya-Araya et al. (2024) revealed an excess of SMGs in $z \gtrsim 2$ protocluster cores

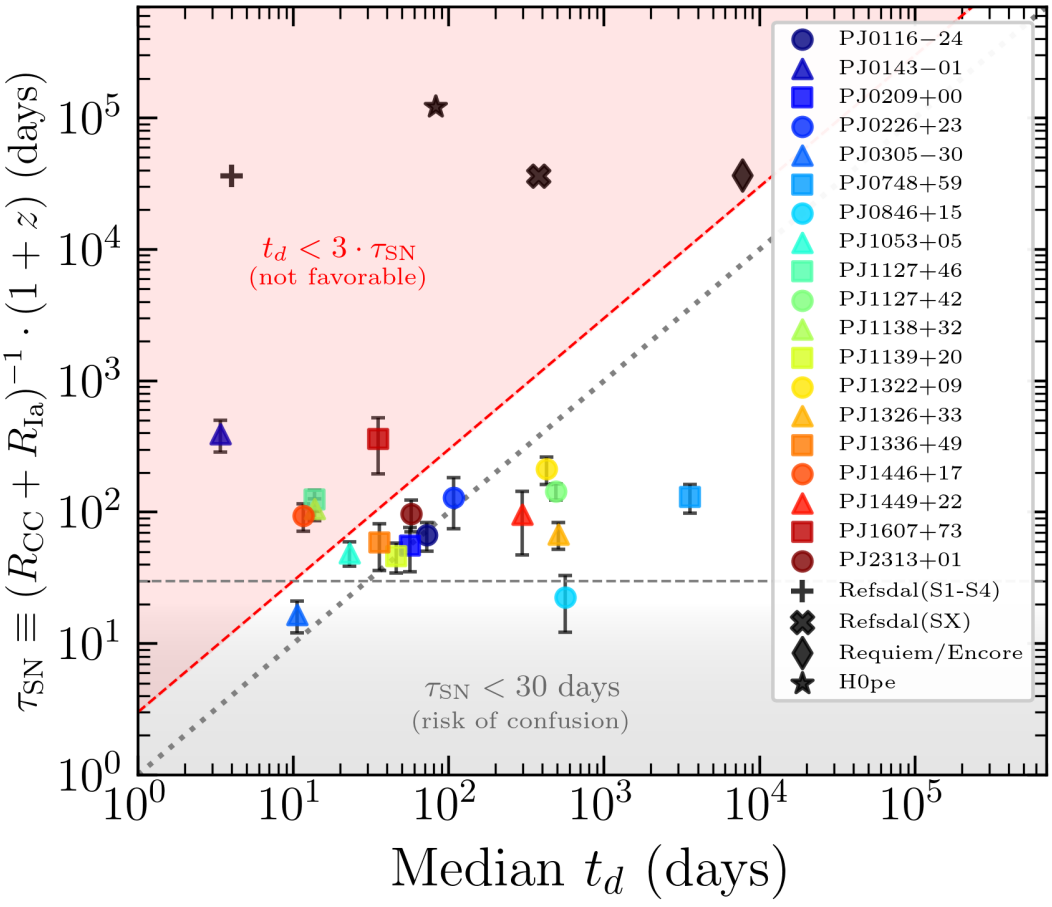

Figure 7. Characteristic timescale between SNe in the observer-frame, $\tau_{\rm SN} \equiv (R_{\rm CC} + R_{\rm Ia})^{-1} \cdot (1+z)$, versus the median time delays t_d for PASSAGES and for glSN host galaxies in the literature. A dotted line indicates $\widetilde{t_d} = \tau_{\rm SN}$, while the red shaded region marks $\widetilde{t_d} < 3 \cdot \tau_{\rm SN}$. We consider this regime not particularly favorable for a sparse monitoring cadence because these target fields are likely to have long stretches with no images of glSNe arriving. On the other hand, targets with a very short $\tau_{\rm SN}$ (e.g., <30 days) carry a risk of confusion in ensuring that SN candidates identified in different arcs are in fact multiple images of the same SN.

(relative to protocluster outskirts or field environments). The authors concluded that this was driven primarily by oversampling the high-mass end of the halo mass function. Fortunately, overdensities of starbursts in protocluster cores (I. Oteo et al. 2018; A. S. Long et al. 2020; J. B. Champagne et al. 2021; S. Arribas et al. 2024) suggest that they may be confined within regions of ∼100–500 kpc in diameter ($\sim 0\farcs2 - 1\farcs0$ at $z = 3$). Thus, they can overlap more substantially with the multiply imaged source-plane regions behind lensing clusters. For example, B. L. Frye et al. (2024) estimated an integrated SFR of 100–500 $M_\odot\,{\rm yr}^{-1}$ in two overdensities ($z \approx 1.8$ and $z \approx 2.2$) behind the G165 cluster, accounting for ∼1–3 CCSNe yr^{-1}. Perhaps as a proof of concept, the triply imaged SN H0pe was discovered in a massive host galaxy within the $z \sim 1.8$ overdensity behind G165 (B. L. Frye et al. 2023, 2024; M. Polletta et al. 2023), through JWST/NIRCam imaging that was primarily targeting the PASSAGES DSFG that is nearby in projection.

4. Summary

So far, discoveries of gravitationally lensed supernovae that can be observed in multiple images have been very limited—unsurprisingly, given that both lensing and SNe are rare phenomena. They are, however, exceptionally useful for the purpose of time-delay cosmography, which depends upon the delays in arrival time between pairs of multiple images (induced by the difference both in path lengths of their respective geodesics and in the gravitational potential that they experience). Considering the yet-unresolved Hubble tension in different measurements of the Universe's expansion rate, novel and independent methods to constrain H_0 are likely to be highly informative. Yet, fewer than 10 multiply imaged SNe have ever been discovered, only two of which have so far been employed successfully for TD cosmography (S. Refsdal and SN H0pe; P. L. Kelly et al. 2023a; M. Pascale et al. 2025). There are several advantages to using SNe for this measurement over, for example, lensed quasars (e.g., reviews by T. Treu et al. 2022; S. Birrer et al. 2024); chief among them is that the light curve of an SN is transient, not just variable like quasars, and is capable of being modeled. For now, though, lensed quasars have a key advantage through being simply more numerous. A joint inference of H_0, combining information from several lensed SNe, can be quite competitive with the level of precision achieved for other methods that have so far received much more attention. To get to this point in the next decade, however, requires many more discoveries, and it will likely not be sufficient to rely on luck alone.

To this end, we consider the feasibility of a targeted approach focused on galaxies that are expected to be uniquely fruitful for gravitationally lensed SNe. In this work, we have

attempted to forecast the rates of glSNe that might be reasonably observed for a set of 21 dusty star-forming galaxies from the PASSAGES sample, spanning $z \approx 1.1$–3.5. Using their magnification-corrected intrinsic SFRs, derived in previous works, we tabulate their rates of CCSNe and Type Ia SNe, $R_{\rm CC}$ and $R_{\rm Ia}$. Given the expectation that only a fraction of this star formation is occurring in regions with low enough dust obscuration to ever be detectable, even with the likes of JWST, we apply an assumed unobscured fraction ($\sim$20%) to our SN rates. The exact sensitivity and control time will depend on observing setup, but I. Mäntynen et al. (2025) found a detectable fraction of $\approx$34% for local LIRGs in an experiment sensitive to $A_V < 16$. We also include the reduction in observable rates due to the fact that time in these galaxies is slowed by a factor of $1 + z$ from the perspective of Earth. On the other hand, the observable rates are boosted by some factor $\mathcal{N}_{\rm eff}$ (capturing the expected value of multiple images that an SN will appear in), based on existing gravitational lens models and the probabilistic distribution of star formation captured by dust and/or radio continuum.

As a result, we estimate a range of intrinsic rates $R_{\rm CC} \approx 1.8$–$65\ {\rm yr}^{-1}$ (CCSNe; median $11\ {\rm yr}^{-1}$) and $R_{\rm Ia} \approx 0.2$–$6.4\ {\rm yr}^{-1}$ (Type Ia; median $1.1\ {\rm yr}^{-1}$), with observable rates $\mathcal{R}_{\rm CC} \approx 0.4 - 8.0\ {\rm yr}^{-1}$ (median $2.3\ {\rm yr}^{-1}$) and $\mathcal{R}_{\rm Ia} \approx 0.2 - 3.9\ {\rm yr}^{-1}$ (median $1.1\ {\rm yr}^{-1}$). As for the time-delayed rates of individual SNe, $R \cdot (1 + z)^{-1}$, we find ranges of 0.8–$20\ {\rm yr}^{-1}$ (median $3.5\ {\rm yr}^{-1}$) and 0.1–$2.0\ {\rm yr}^{-1}$ (median $0.3\ {\rm yr}^{-1}$) for CCSNe and SNe Ia, respectively. The number of SNe that a monitoring campaign would yield is dependent on the control time of the observations or the duration for which a given SN would be above survey limits. In this regard, the biggest challenge for this particular sample would be ensuring adequate near-infrared sensitivity to withstand dust attenuation, effectively necessitating JWST/NIRCam. While we have discussed some evidence that the attenuation might be inhomogeneous enough to allow some relatively unobscured sightlines, this is a source of large uncertainty at the moment.

Despite this challenge, the population of lensed starbursts is a veritable wealth of SNe, in the extremely rarefied stratum of galaxies with more than one SN occurring per (rest-frame) year. Notwithstanding sheer luck, for almost any other targeted strategy to discover glSNe, it would be necessary to monitor either a small sample for several years, or else a very large sample over a shorter timespan. Whereas only three glSNe have yet delivered time-delay cosmographical measurements (S. Refsdal, SN H0pe, and SN Encore, at time of writing), every new discovery has enormous potential to significantly improve the level of uncertainty on H_0 inferences and other cosmological parameters (e.g., C. Grillo et al. 2024). The ultimate goal of the next decade is to reach $\sim$1% precision through joint inference (D. Coe & L. A. Moustakas 2009; T. Treu & P. J. Marshall 2016; T. Treu et al. 2022).

Fortunately, the PASSAGES objects typically have wider separations between lensed images; their Einstein radii satisfy $\theta_{\rm Ein} \gtrsim 0\farcs5$ in the vast majority of cases, with some even exceeding $10''$. We find that a strong correlation between $\theta_{\rm Ein}$ and their median lens model-predicted time delays, which may even have some analytical basis connecting the maximum time delay that can be expected for an axisymmetric isothermal lens and its Einstein radius (Appendix B). Finally, we compare the expected median time delays to the characteristic observed-frame timescale between SN events (including both CCSNe and Type Ia). We find that PASSAGES occupies an ideal regime where the lensing time delays are not significantly shorter than the time between individual SNe, such that multiple imaging from lensing helps improve the odds of catching one in a random monitoring program.

While this work forecasts the potential of the $\sim$30 PASSAGES lensed DSFGs, in part because they account for a non-negligible fraction of the known HyLIRGs, there are several hundred other candidate lensed DSFGs known currently, and perhaps many thousand more yet to be discovered at slightly lower intrinsic luminosities (C. Sedgwick et al. 2025). We contend that an optimal approach would involve targeted searches in tandem with (ongoing and planned) wide-area and blind surveys with Euclid, Rubin LSST, the China Space Station Telescope, and the Roman Space Telescope (e.g., D. A. Goldstein & P. E. Nugent 2017; D. A. Goldstein et al. 2019; R. Wojtak et al. 2019; J. D. R. Pierel et al. 2021; D. Ryczanowski et al. 2023; A. Sainz de Murieta et al. 2023, 2024; N. Arendse et al. 2024; J. Dong et al. 2024; M. Bronikowski et al. 2025).

The level of precision in H_0 measurements from cluster-lensed SNe has been of order 6%–7% for S. Refsdal (C. Grillo et al. 2018; P. L. Kelly et al. 2023a) and 7%–13% for SN H0pe (M. Pascale et al. 2025). While it will not be possible to replicate the fully blinded process used in obtaining these results, there is a distinct possibility in refining these uncertainties. For example, the lens models for SN H0pe were constructed with only five spectroscopically confirmed image system redshifts (out of 21), which can have a sizeable influence on model accuracy (e.g., T. L. Johnson & K. Sharon 2016). Similarly, the SN H0pe inference was subject to unique photometric uncertainties at the time of publication due to the lack of a "template" image (where the SN was not visible) of the host galaxy in most filters (J. D. R. Pierel et al. 2024a). The images of SN Encore with the shortest time delays are similarly expected to yield a measurement of order $\approx$10% precision, whereas the longest delays (>3000 days) could reduce this to 2%–3% (J. D. R. Pierel et al. 2024b; S. Suyu et al. 2025; J. D. R. Pierel et al. 2026).

Within PASSAGES, five cluster fields have estimated median time delays exceeding 100 days and $\theta_{\rm Ein} > 5''$ (PJ0748+59, PJ0846+15, PJ1127+42, PJ1322+09, and PJ1449+22) and should in principle offer the greatest likelihood of a similar level of precision if glSNe were discovered in each. A joint population inference for $\sim$20 lensed SNe has the potential to reach $\sim$1% level precision on H_0 (S. H. Suyu et al. 2020), but even a sample of only six lensed quasars has been able to reach high relative uncertainty. K. C. Wong et al. (2020) presented a precision of $\sim$2%, although later works showed that systematic uncertainties for these galaxy-scale lens systems were likely underestimated by around a factor of 2 (e.g., S. Birrer et al. 2020; K. Blum et al. 2020; C. S. Kochanek 2020; P. Denzel et al. 2021; C. S. Kochanek 2021). Spatially resolved kinematics and other external information on the foreground lenses have returned the precision to $\sim$2%, with an ultimate goal toward 1% from the Time-Delay COSMOgraphy (TDCOSMO) collaboration (S. Birrer & T. Treu 2021; A. J. Shajib et al. 2023; TDCOSMO Collaboration et al. 2025). The discovery of five lensed SNe suitable for cosmography from a sample such as PASSAGES —especially for cluster-scale systems— would result in a competitive H_0 measurement, shedding much-needed light on the Hubble tension.

Acknowledgments

P.S.K. would like to thank Haojing Yan, Ian Smail, Kate Whitaker, and Kevin Croker for helpful discussions related to this work. P.S.K. acknowledges financial support from the Knut and Alice Wallenberg Foundation. R.A.W., S.H.C., and R.A.J. acknowledge support from NASA JWST Interdisciplinary Scientist grants NAG5-12460, NNX14AN10G, and 80NSSC18K0200 from GSFC. T.C. acknowledges support from the Beus Center for Cosmic Foundations. E.F.-J.A. acknowledges support from UNAM-PAPIIT project IA102023 and from CONAHCyT Ciencia de Frontera project ID: CF-2023-I-506.

This paper makes use of the following ALMA data: ADS/JAO.ALMA #2015.1.01518.S, #2017.1.01214.S, #2016.1.00048.S, and #2019.1.01636.S. ALMA is a partnership of ESO (representing its member states), NSF (USA) and NINS (Japan), together with NRC (Canada), MOST and ASIAA (Taiwan), and KASI (Republic of Korea), in cooperation with the Republic of Chile. The Joint ALMA Observatory is operated by ESO, AUI/NRAO and NAOJ. The National Radio Astronomy Observatory is a facility of the National Science Foundation operated under cooperative agreement by Associated Universities, Inc. This research has made extensive use of NASA's Astrophysics Data System.

This work utilizes gravitational lensing models produced by PIs Bradač, Natarajan and Kneib (CATS), Merten and Zitrin, Sharon, Williams, Keeton, Bernstein and Diego, and the GLAFIC group. This lens modeling was partially funded by the HST Frontier Fields program conducted by STScI. STScI is operated by the Association of Universities for Research in Astronomy, Inc. under NASA contract NAS 5-26555. The lens models were obtained from the Mikulski Archive for Space Telescopes (MAST).

We also acknowledge the indigenous peoples of Arizona, including the Akimel O'odham (Pima) and Pee Posh (Maricopa) Indian Communities, whose care and keeping of the land has enabled us to be at ASU's Tempe campus in the Salt River Valley, where much of our work was conducted.

Facilities: ALMA, VLA.

Software: APLPY (T. Robitaille & E. Bressert 2012; T. Robitaille 2019), ASTROPY (Astropy Collaboration et al. 2013, 2018, 2022), BLOBCAT (C. A. Hales et al. 2012), CASA (J. P. McMullin et al. 2007), LENSTOOL (J. P. Kneib et al. 1993; J.-P. Kneib et al. 1996; E. Jullo et al. 2007; E. Jullo & J.-P. Kneib 2009), matplotlib (J. D. Hunter 2007), pandas (W. McKinney 2010; The pandas Development Team 2024), Ned Wright's Cosmology Calculator (E. L. Wright 2006)

Appendix A
Estimating SNe Ia Rates Robustly Without Stellar Mass Measurements

For a subset of the PASSAGES sample, P. S. Kamieneski et al. (2024a) made predictions for the sSFRs relative to the SFMS of galaxies between SFR and $M_\star$ (e.g., J. Brinchmann et al. 2004; E. Daddi et al. 2007; K. E. Whitaker et al. 2012; J. S. Speagle et al. 2014). P. S. Kamieneski et al. (2024a) used the objects' gas depletion times (∼150–350 Myr; K. C. Harrington et al. 2016, 2021; D. A. Berman et al. 2022) to estimate that they occupied the regime of $\Delta\mathrm{MS} \equiv \log_{10}(\mathrm{SFR}/\mathrm{SFR_{MS}}) \approx 0.0 - 0.9$, following the prescription of T.-M. Wang et al. 2022 (see also R. Genzel et al. 2015; L. J. Tacconi et al. 2018; D. Liu et al. 2019). In an independent approach, P. S. Kamieneski et al. (2024a) used SFR surface densities Σ_{SFR} to estimate ΔMS, as per E. F. Jiménez-Andrade et al. (2019), resulting in a range of $\Delta\mathrm{MS} \approx -0.1$–0.5.

With this information in mind, a sensible upper limit for their sSFRs would be $\Delta\mathrm{MS} < 0.9$ dex, which happens to be ≈3 times the 1σ scatter of the main sequence and also 0.3 dex above the typical threshold for starburst galaxies (G. Rodighiero et al. 2011). To further motivate this, we consider some recent measurements of stellar masses in large samples of DSFGs. O. Miettinen et al. (2017) found that 57% of a sample of 124 mm selected DSFGs in COSMOS were within a factor of 3 (≈0.5 dex) of the main sequence and 89% were below $\Delta\mathrm{MS} < 0.9$ dex. Similarly, for 185 submillmeter selected DSFGs in the North Ecliptic Pole (NEP) field, L. Barrufet et al. (2020) found 57% within 0.5 dex of the main sequence. More recently, in a large sample of ≈ 450 $z > 1$ sources in the NEP selected at 850 μm, H. Shim et al. (2022) found 67% with $\Delta\mathrm{MS} < 0.5$ dex and 90% with $\Delta\mathrm{MS} < 0.9$ dex.[26] For 707 DSFGs in AS2UDS, U. Dudzevičiūtė et al. (2020) found 66% ± 3% satisfied with $\Delta\mathrm{MS} < 0.6$ dex. This finding that DSFGs are largely not dramatically above the main sequence—with apparently the majority even consistent with the SFMS—is not particularly surprising. As discussed by C. M. Casey et al. (2014a), the duty cycle of DSFGs in the starburst regime ($\Delta_{\mathrm{MS}} > 0.6$ dex) might be quite short, so that they spend most of their time on the main sequence.

We can use this upper limit in sSFR of 0.9 dex above the main sequence (computed according to J. S. Speagle et al. 2014), along with the total SFRs inferred from the infrared, in order to derive lower limits in $M_\star$. We also use a lower limit of sSFR 0.3 dex below the SFMS, giving the upper limits in $M_\star$. By extension, these provide lower and upper limits, respectively, in the SNe Ia rate, R_{Ia}. Fortunately, as illustrated in Equation (8), the dependence on $M_\star$ is quite weak relative to SFR for galaxies on or above the main sequence, so these approximate limits contribute extremely minimally to the error budget in comparison with the uncertainties on SFR.

Appendix B
The Connection between Typical Time Delays and Image Separations

As noted by H. J. Witt et al. (2000) and M. Oguri (2007), a lens with an isothermal potential $\phi(r, \theta) = r \cdot F(\theta)$ for generalized angular structure $F(\theta)$ will result in time delays between arcs i and j

$$\Delta t_{ij} = \frac{1 + z_l}{2c} \frac{D_L D_S}{D_{LS}} (r_j^2 - r_i^2) \tag{B1}$$

where r_i is the angular distance from arc i to the center of the lens. This produces the result that r_j and r_i can be arbitrarily large—and therefore θ_{Ein} as well—and still produce a small time delay, as long as $r_j \approx r_i$. In addition, at the redshift of the lens, the physical separation between deflected light rays is $R_{\mathrm{Ein}} = D_L \cdot \theta_{\mathrm{Ein}}$. Considering the maximum possible TDs in this formulation (holding fixed the lens and source redshift),

$$\max(\Delta t_{ij}) \propto \max(r_j^2 - r_i^2) \propto (R_{\mathrm{Ein}})^2. \tag{B2}$$

[26] As a caveat, both L. Barrufet et al. and H. Shim et al. lacked resolved submillimeter imaging.

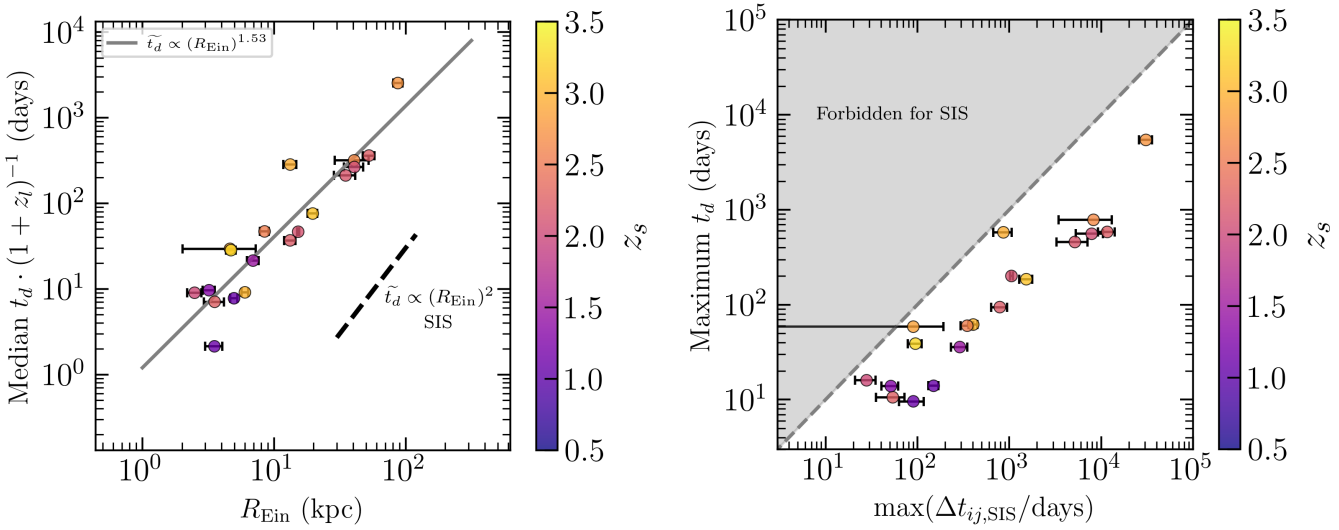

Figure 8. (Left) Figure 6 is modified to now plot the median time delays t_d of PASSAGES at the redshift of the lens—i.e., including a dilation factor of $(1+z_l)^{-1}$—versus the physical Einstein radius $R_{\rm Ein} = D_L \cdot \theta_{\rm Ein}$. A gray line shows the best-fit power law, $\widetilde{t_d} \propto (R_{\rm Ein})^{1.53\pm0.16}$, while the dashed line segment shows the approximate scaling relation for a singular isothermal spheroid (SIS) lens with a power-law slope of 2. The colorscale shows source-plane redshift. (Right) Now, the maximum time delays versus the predicted $\max(\Delta t_{\rm ij})$ computed based on the redshift geometries and $\theta_{\rm Ein}$ according to Equation (B5). The quasi-forbidden region (where lens model-predicted maximum time delays exceed the values allowed for an SIS lens at the respective lens/source redshifts with the respective Einstein radii), $\max(t_d) > \max(\Delta t_{ij,\rm SIS})$ is shown shaded in gray.

In the left panel of Figure 8, we modify Figure 6 to show $R_{\rm Ein}$ (in kpc) on the horizontal axis and the median time delay, dilated to the redshift of the lens with a $(1+z_l)^{-1}$ factor. The best-fit power-law slope for the median time delays is $\widetilde{t_d} \propto (R_{\rm Ein})^{1.53\pm0.16}$, slightly shallower than the prediction for the maximum time delays.

In at least the specific case of a singular isothermal spheroid (SIS) lens, the two images satisfy

$$r_j^2 - r_i^2 = (\theta_{\rm Ein} + \beta)^2 - (\theta_{\rm Ein} - \beta)^2 = 4\theta_{\rm Ein}\beta \qquad \text{(B3)}$$

for source-plane offset β relative to the lens centroid (R. Narayan & M. Bartelmann 1996). By necessity, $\beta < \theta_{\rm Ein}$, or else only a single image appears. Therefore,

$$\max(r_j^2 - r_i^2) = 4\theta_{\rm Ein}^2 \qquad \text{(B4)}$$

and

$$\max(\Delta t_{ij}) = \frac{1+z_l}{2c}\frac{D_L D_S}{D_{LS}} \cdot 4\theta_{\rm Ein}^2 \qquad \text{(B5)}$$

for an SIS lens, with $\theta_{\rm Ein}$ in radians. The right panel of Figure 8 plots this term on the horizontal axis, with the maximum time delays predicted by the lens model (Table 2) on the vertical axis. A quasi-forbidden region is shaded in gray, representing model-predicted time delays that exceed the maximum from the H. J. Witt et al. (2000) and M. Oguri (2007) equation in the case of an SIS. We observe that the maximum model-predicted time delays t_d remain below $\max(\Delta t_{ij})$.

Given the limiting assumptions implicit to this formulation (mainly that the lensing mass is consistent with a single SIS lens), this connection between time delays and Einstein radii will not hold in all cases. Still, it is reasonably useful for our purposes in identifying lenses that are more likely to have time delays of order months to years. By Equation (B5), for a fiducial SIS lens at $z_l = 0.5$ and source at $z_s = 2$, $\max(\Delta t_{ij}) < 30$ days for $\theta_{\rm Ein} \lesssim 0\farcs4$, while $\max(\Delta t_{ij}) < 100$ days for $\theta_{\rm Ein} \lesssim 0\farcs8$. Only ∼29% of the PASSAGES subsample have $\theta_{\rm Ein} < 0\farcs8$ (Table 2), while none considered have $\theta_{\rm Ein} < 0\farcs4$, so their time delays are more likely to be longer, which generally yields improved H_0 precision.

ORCID iDs

Patrick S. Kamieneski https://orcid.org/0000-0001-9394-6732
Rogier A. Windhorst https://orcid.org/0000-0001-8156-6281
Brenda L. Frye https://orcid.org/0000-0003-1625-8009
Min S. Yun https://orcid.org/0000-0001-7095-7543
Kevin C. Harrington https://orcid.org/0000-0001-5429-5762
Simon D. Mork https://orcid.org/0000-0002-5573-9131
Nicholas Foo https://orcid.org/0000-0002-7460-8460
Nikhil Garuda https://orcid.org/0000-0003-3418-2482
Massimo Pascale https://orcid.org/0000-0002-2282-8795
Belén Alcalde Pampliega https://orcid.org/0000-0002-4140-0428
Timothy Carleton https://orcid.org/0000-0001-6650-2853
Seth H. Cohen https://orcid.org/0000-0003-3329-1337
Carlos Garcia Diaz https://orcid.org/0000-0002-4223-2016
Rolf A. Jansen https://orcid.org/0000-0003-1268-5230
Eric F. Jiménez-Andrade https://orcid.org/0000-0002-2640-5917
Anton M. Koekemoer https://orcid.org/0000-0002-6610-2048
James D. Lowenthal https://orcid.org/0000-0001-9969-3115
Allison Noble https://orcid.org/0000-0003-1832-4137
Justin D. R. Pierel https://orcid.org/0000-0002-2361-7201
Amit Vishwas https://orcid.org/0000-0002-4444-8929
Q. Daniel Wang https://orcid.org/0000-0002-9279-4041
Ilsang Yoon https://orcid.org/0000-0001-9163-0064

References

Aalto, S., Martín, S., Costagliola, F., et al. 2015, A&A, 584, A42
Abdurro'uf, Coe, D., Jung, I., et al. 2023, ApJ, 945, 117
Aiola, S., Calabrese, E., Maurin, L., et al. 2020, JCAP, 2020, 047
Akins, H. B., Casey, C. M., Champagne, J. B., et al. 2025, arXiv:2508.06607
Alberts, S., & Noble, A. 2022, Univ, 8, 554
Amodeo, S., Mei, S., Stanford, S. A., et al. 2018, ApJ, 853, 36
Anand, G. S., Riess, A. G., Yuan, W., et al. 2024, ApJ, 966, 89
Andersen, P., & Hjorth, J. 2018, MNRAS, 480, 68
Araya-Araya, P., Cochrane, R. K., Hayward, C. C., et al. 2024, ApJ, 977, 204
Arendse, N., Dhawan, S., Sagués Carracedo, A., et al. 2024, MNRAS, 531, 3509
Arribas, S., Perna, M., Rodríguez Del Pino, B., et al. 2024, A&A, 688, A146
Astropy Collaboration, Price-Whelan, A. M., Lim, P. L., et al. 2022, ApJ, 935, 167
Astropy Collaboration, Price-Whelan, A. M., Sipőcz, B. M., et al. 2018, AJ, 156, 123
Astropy Collaboration, Robitaille, T. P., Tollerud, E. J., et al. 2013, A&A, 558, A33
Bag, S., Huber, S., Suyu, S. H., et al. 2024, A&A, 691, A100
Baker, W. M., Maiolino, R., Bluck, A. F. L., et al. 2022, MNRAS, 510, 3622
Bakx, T. J. L. C., Amvrosiadis, A., Bendo, G. J., et al. 2024a, MNRAS, 535, 1533
Bakx, T. J. L. C., Eales, S. A., Negrello, M., et al. 2018, MNRAS, 473, 1751
Bakx, T. J. L. C., Gray, B. S., González-Nuevo, J., et al. 2024b, MNRAS, 527, 8865
Barrufet, L., Pearson, C., Serjeant, S., et al. 2020, A&A, 641, A129
Bellm, E. 2014, in The Third Hot-wiring the Transient Universe Workshop (HTU-III), ed. P. R. Wozniak et al. (CalTech), 27
Berman, D. A., Yun, M. S., Harrington, K. C., et al. 2022, MNRAS, 515, 3911
Bik, A., Östlin, G., Menacho, V., et al. 2018, A&A, 619, A131
Birrer, S., Millon, M., Sluse, D., et al. 2024, SSRv, 220, 48
Birrer, S., Shajib, A. J., Galan, A., et al. 2020, A&A, 643, A165
Birrer, S., & Treu, T. 2021, A&A, 649, A61
Blain, A. W. 1996, MNRAS, 283, 1340
Blandford, R. D., & Narayan, R. 1992, ARA&A, 30, 311
Blum, K., Castorina, E., & Simonović, M. 2020, ApJL, 892, L27
Bondi, M., Pérez-Torres, M. A., Herrero-Illana, R., & Alberdi, A. 2012, A&A, 539, A134
Bonvin, V., Courbin, F., Suyu, S. H., et al. 2017, MNRAS, 465, 4914
Boquien, M., Calzetti, D., Kennicutt, R., et al. 2009, ApJ, 706, 553
Borsato, E., Marchetti, L., Negrello, M., et al. 2024, MNRAS, 528, 6222
Bournaud, F., Elmegreen, B. G., & Elmegreen, D. M. 2007, ApJ, 670, 237
Brinchmann, J., Charlot, S., White, S. D. M., et al. 2004, MNRAS, 351, 1151
Bronikowski, M., Petrushevska, T., Pierel, J. D. R., et al. 2025, A&A, 697, A146
Bussmann, R. S., Pérez-Fournon, I., Amber, S., et al. 2013, ApJ, 779, 25
Cañameras, R., Nesvadba, N. P. H., Guery, D., et al. 2015, A&A, 581, A105
Cañameras, R., Nesvadba, N. P. H., Limousin, M., et al. 2018, A&A, 620, A60
Calvi, R., Castignani, G., & Dannerbauer, H. 2023, A&A, 678, A15
Calzetti, D. 1997, AIPC, 408, 403
Calzetti, D., Armus, L., Bohlin, R. C., et al. 2000, ApJ, 533, 682
Capak, P. L., Riechers, D., Scoville, N. Z., et al. 2011, Natur, 470, 233
Casey, C. M. 2016, ApJ, 824, 36
Casey, C. M., Cooray, A., Capak, P., et al. 2015, ApJL, 808, L33
Casey, C. M., Cooray, A., Killi, M., et al. 2017, ApJ, 840, 101
Casey, C. M., Narayanan, D., & Cooray, A. 2014a, PhR, 541, 45
Casey, C. M., Scoville, N. Z., Sanders, D. B., et al. 2014b, ApJ, 796, 95
Chabrier, G. 2003, PASP, 115, 763
Champagne, J. B., Casey, C. M., Zavala, J. A., et al. 2021, ApJ, 913, 110
Chen, C.-C., Harrison, C. M., Smail, I., et al. 2020, A&A, 635, A119
Chen, W., Kelly, P. L., Frye, B. L., et al. 2024, ApJ, 970, 102
Chen, W., Kelly, P. L., Oguri, M., et al. 2022, Natur, 611, 256
Cheng, C., Ibar, E., Smail, I., et al. 2020, MNRAS, 499, 5241
Chevance, M., Kruijssen, J. M. D., Hygate, A. P. S., et al. 2020, MNRAS, 493, 2872
Chevance, M., Kruijssen, J. M. D., Krumholz, M. R., et al. 2022, MNRAS, 509, 272
Chiang, Y.-K., Overzier, R., & Gebhardt, K. 2013, ApJ, 779, 127
Chornock, R., Berger, E., Rest, A., et al. 2013, ApJ, 767, 162
Clarke, C., & Oey, M. S. 2002, MNRAS, 337, 1299
Clements, D. L., Braglia, F., Petitpas, G., et al. 2016, MNRAS, 461, 1719
Coe, D., & Moustakas, L. A. 2009, ApJ, 706, 45
Condon, J. J. 1992, ARA&A, 30, 575
Cooper, O. R., Brammer, G., Heintz, K. E., et al. 2025, ApJ, 982, 125
Cortese, L., Boselli, A., Buat, V., et al. 2006, ApJ, 637, 242
Courbin, F., Bonvin, V., Buckley-Geer, E., et al. 2018, A&A, 609, A71
Courbin, F., Eigenbrod, A., Vuissoz, C., Meylan, G., & Magain, P. 2005, IAUS, 225, 297
Craig, P., O'Connor, K., Chakrabarti, S., et al. 2024, MNRAS, 534, 1077
Cresci, G., Mannucci, F., Della Valle, M., & Maiolino, R. 2007, A&A, 462, 927
Daddi, E., Dannerbauer, H., Stern, D., et al. 2009, ApJ, 694, 1517
Daddi, E., Dickinson, M., Morrison, G., et al. 2007, ApJ, 670, 156
Dahle, H., Gladders, M. D., Sharon, K., Bayliss, M. B., & Rigby, J. R. 2015, ApJ, 813, 67
Dahlen, T., Strolger, L.-G., Riess, A. G., et al. 2012, ApJ, 757, 70
Dannerbauer, H., Kurk, J. D., De Breuck, C., et al. 2014, A&A, 570, A55
De Breuck, C., Bertoldi, F., Carilli, C., et al. 2004, A&A, 424, 1
de Grijs, R., Anders, P., Bastian, N., et al. 2003, MNRAS, 343, 1285
Dekel, A., Sari, R., & Ceverino, D. 2009, ApJ, 703, 785
Del Moro, A., Alexander, D. M., Mullaney, J. R., et al. 2013, A&A, 549, A59
Delvecchio, I., Smolčić, V., Zamorani, G., et al. 2017, A&A, 602, A3
Denzel, P., Coles, J. P., Saha, P., & Williams, L. L. R. 2021, MNRAS, 501, 784
Dhawan, S., Johansson, J., Goobar, A., et al. 2020, MNRAS, 491, 2639
Díaz-Sánchez, A., Iglesias-Groth, S., Rebolo, R., & Dannerbauer, H. 2017, ApJL, 843, L22
Diego, J. M., Bernstein, G., Chen, W., et al. 2022, A&A, 662, A34
Domínguez Sánchez, H., Mignoli, M., Pozzi, F., et al. 2012, MNRAS, 426, 330
Dong, J., Shu, Y., Li, G., et al. 2024, A&A, 689, A192
Donley, J. L., Rieke, G. H., Rigby, J. R., & Pérez-González, P. G. 2005, ApJ, 634, 169
Drake, A. B., Walter, F., Novak, M., et al. 2020, ApJ, 902, 37
Dudzevičiūtė, U., Smail, I., Swinbank, A. M., et al. 2020, MNRAS, 494, 3828
Emig, K. L., Bolatto, A. D., Leroy, A. K., et al. 2020, ApJ, 903, 50
Ertl, S., Suyu, S. H., Schuldt, S., et al. 2025, A&A, 702, A157
Euclid Collaboration, Scaramella, R., Amiaux, J., et al. 2022, A&A, 662, A112
Faisst, A. L., Capak, P. L., Yan, L., et al. 2017, ApJ, 847, 21
Faisst, A. L., Yang, L., Brinch, M., et al. 2025, ApJ, 980, 204
Falco, E. E., Gorenstein, M. V., & Shapiro, I. I. 1985, ApJL, 289, L1
Falstad, N., Aalto, S., König, S., et al. 2021, A&A, 649, A105
Fohlmeister, J., Kochanek, C. S., Falco, E. E., Morgan, C. W., & Wambsganss, J. 2008, ApJ, 676, 761
Fohlmeister, J., Kochanek, C. S., Falco, E. E., et al. 2007, ApJ, 662, 62
Foo, N., Harrington, K. C., Frye, B. L., et al. 2025, ApJ, 995, 219
Fox, O. D., Khandrika, H., Rubin, D., et al. 2021, MNRAS, 506, 4199
Freedman, W. L., Madore, B. F., Hatt, D., et al. 2019, ApJ, 882, 34
Freedman, W. L., Madore, B. F., Hoyt, T. J., et al. 2025, ApJ, 985, 203
Frye, B. L., Pascale, M., Cohen, S., et al. 2023, TNSAN, 96, 1
Frye, B. L., Pascale, M., Pierel, J., et al. 2024, ApJ, 961, 171
Frye, B. L., Pascale, M., Qin, Y., et al. 2019, ApJ, 871, 51
Fujimoto, S., Ouchi, M., Kohno, K., et al. 2025, NatAs, 9, 1553
Fujimoto, S., Ouchi, M., Shibuya, T., & Nagai, H. 2017, ApJ, 850, 83
Gal-Yam, A., Maoz, D., & Sharon, K. 2002, MNRAS, 332, 37
Genzel, R., Tacconi, L. J., Lutz, D., et al. 2015, ApJ, 800, 20
Giménez-Arteaga, C., Oesch, P. A., Brammer, G. B., et al. 2023, ApJ, 948, 126
Giulietti, M., Gandolfi, G., Massardi, M., Behiri, M., & Lapi, A. 2024, Galax, 12, 9
Goldstein, D. A., & Nugent, P. E. 2017, ApJL, 834, L5
Goldstein, D. A., Nugent, P. E., & Goobar, A. 2019, ApJS, 243, 6
Goobar, A., Amanullah, R., Kulkarni, S. R., et al. 2017, Sci, 356, 291
Goobar, A., Johansson, J., Schulze, S., et al. 2023, NatAs, 7, 1098
Goobar, A. A., Johansson, J., Dhawan, S., et al. 2022, TNSAN, 180, 1
Gorenstein, M. V., Falco, E. E., & Shapiro, I. I. 1988, ApJ, 327, 693
Greve, T. R., Bertoldi, F., Smail, I., et al. 2005, MNRAS, 359, 1165
Grillo, C., Pagano, L., Rosati, P., & Suyu, S. H. 2024, A&A, 684, L23
Grillo, C., Rosati, P., Suyu, S. H., et al. 2018, ApJ, 860, 94
Gullberg, B., Smail, I., Swinbank, A. M., et al. 2019, MNRAS, 490, 4956
Hales, C. A., Murphy, T., Curran, J. R., et al. 2012, MNRAS, 425, 979
Harrington, K. C., Weiss, A., Yun, M. S., et al. 2021, ApJ, 908, 95
Harrington, K. C., Yun, M. S., Cybulski, R., et al. 2016, MNRAS, 458, 4383
Harvey, T., Conselice, C. J., Adams, N. J., et al. 2025, MNRAS, 542, 2998
Hezaveh, Y. D., Marrone, D. P., & Holder, G. P. 2012, ApJ, 761, 20
Hickox, R. C., Wardlow, J. L., Smail, I., et al. 2012, MNRAS, 421, 284
Hilbert, S., White, S. D. M., Hartlap, J., & Schneider, P. 2007, MNRAS, 382, 121

Hilbert, S., White, S. D. M., Hartlap, J., & Schneider, P. 2008, MNRAS, 386, 1845
Hodge, J. A., Smail, I., Walter, F., et al. 2019, ApJ, 876, 130
Hodge, J. A., Swinbank, A. M., Simpson, J. M., et al. 2016, ApJ, 833, 103
Holwerda, B. W., Knabel, S., Steele, R. C., et al. 2021, MNRAS, 505, 1316
Hounsell, R., Scolnic, D., Foley, R. J., et al. 2018, ApJ, 867, 23
Huber, S., Suyu, S. H., Ghoshdastidar, D., et al. 2022, A&A, 658, A157
Huber, S., Suyu, S. H., Noebauer, U. M., et al. 2019, A&A, 631, A161
Hung, C.-L., Casey, C. M., Chiang, Y.-K., et al. 2016, ApJ, 826, 130
Hunter, J. D. 2007, CSE, 9, 90
Immeli, A., Samland, M., Gerhard, O., & Westera, P. 2004, A&A, 413, 547
Irwin, M. J., Webster, R. L., Hewett, P. C., Corrigan, R. T., & Jedrzejewski, R. 1989, AJ, 98, 1989
Jarrett, T. H., Masci, F., Tsai, C. W., et al. 2013, AJ, 145, 6
Jencson, J. E., Kasliwal, M. M., Adams, S. M., et al. 2019, ApJ, 886, 40
Ji, Z., Alberts, S., Zhu, Y., et al. 2025, ApJL, 988, L69
Jiménez-Andrade, E. F., Magnelli, B., Karim, A., et al. 2019, A&A, 625, A114
Johnson, T. L., & Sharon, K. 2016, ApJ, 832, 82
Jullo, E., & Kneib, J.-P. 2009, MNRAS, 395, 1319
Jullo, E., Kneib, J.-P., Limousin, M., et al. 2007, NJPh, 9, 447
Kalita, B. S., Silverman, J. D., Daddi, E., et al. 2025, MNRAS, 537, 402
Kamieneski, P. S. 2024, IAUS, 381, 147
Kamieneski, P. S., Frye, B. L., Windhorst, R. A., et al. 2024b, ApJ, 973, 25
Kamieneski, P. S., Yun, M. S., Harrington, K. C., et al. 2024a, ApJ, 961, 2
Kankare, E., Efstathiou, A., Kotak, R., et al. 2021, A&A, 649, A134
Kankare, E., Mattila, S., Ryder, S., et al. 2008, ApJL, 689, L97
Kankare, E., Mattila, S., Ryder, S., et al. 2012, ApJL, 744, L19
Kauffmann, G., Colberg, J. M., Diaferio, A., & White, S. D. M. 1999, MNRAS, 307, 529
Keeton, C. R., Falco, E. E., Impey, C. D., et al. 2000, ApJ, 542, 74
Kelly, P. L., Rodney, S., Treu, T., et al. 2023a, Sci, 380, abh1322
Kelly, P. L., Rodney, S., Treu, T., et al. 2023b, ApJ, 948, 93
Kelly, P. L., Rodney, S. A., Treu, T., et al. 2015, Sci, 347, 1123
Kelly, P. L., Rodney, S. A., Treu, T., et al. 2016, ApJL, 819, L8
Kennicutt, R. C. J. 1998, ApJ, 498, 541
Kewley, L. J., Geller, M. J., Jansen, R. A., & Dopita, M. A. 2002, AJ, 124, 3135
Kim, C.-G., & Ostriker, E. C. 2015, ApJ, 802, 99
Kneib, J.-P., Ellis, R. S., Smail, I., Couch, W. J., & Sharples, R. M. 1996, ApJ, 471, 643
Kneib, J. P., Mellier, Y., Fort, B., & Mathez, G. 1993, A&A, 273, 367
Kochanek, C. S. 2002, ApJ, 578, 25
Kochanek, C. S. 2020, MNRAS, 493, 1725
Kochanek, C. S. 2021, MNRAS, 501, 5021
Kool, E. C., Ryder, S., Kankare, E., et al. 2018, MNRAS, 473, 5641
Koopmans, L. V. E., Treu, T., Fassnacht, C. D., Blandford, R. D., & Surpi, G. 2003, ApJ, 599, 70
Kroupa, P. 2001, MNRAS, 322, 231
Lee, A. J., Freedman, W. L., Madore, B. F., et al. 2021, ApJ, 907, 112
Leitet, E., Bergvall, N., Hayes, M., Linné, S., & Zackrisson, E. 2013, A&A, 553, A106
Levy, R. C., Bolatto, A. D., Mayya, D., et al. 2024, ApJL, 973, L55
Lewis, A. J. R., Ivison, R. J., Best, P. N., et al. 2018, ApJ, 862, 96
Liang, L., Feldmann, R., Hayward, C. C., et al. 2021, MNRAS, 502, 3210
Linden, S. T., Evans, A. S., Rich, J., et al. 2017, ApJ, 843, 91
Liu, D., Förster Schreiber, N. M., Harrington, K. C., et al. 2024, NatAs, 8, 1181
Liu, D., Schinnerer, E., Groves, B., et al. 2019, ApJ, 887, 235
Liu, Z., Silverman, J. D., Daddi, E., et al. 2024, ApJ, 968, 15
Long, A. S., Cooray, A., Ma, J., et al. 2020, ApJ, 898, 133
Lonsdale, C. J., Diamond, P. J., Thrall, H., Smith, H. E., & Lonsdale, C. J. 2006, ApJ, 647, 185
Lotz, J. M., Koekemoer, A., Coe, D., et al. 2017, ApJ, 837, 97
Louis, T., La Posta, A., Atkins, Z., et al. 2025, JCAP, 2025, 062
LSST Science Collaboration, Abell, P. A., Allison, J., et al. 2009, arXiv:0912.0201
Lucas, W. E., Bonnell, I. A., & Dale, J. E. 2020, MNRAS, 493, 4700
Madau, P., della Valle, M., & Panagia, N. 1998, MNRAS, 297, L17
Madau, P., & Dickinson, M. 2014, ARA&A, 52, 415
Magee, M. R., Sainz de Murieta, A., Collett, T. E., & Enzi, W. 2023, MNRAS, 525, 542
Mannucci, F., Della Valle, M., & Panagia, N. 2006, MNRAS, 370, 773
Mannucci, F., Della Valle, M., Panagia, N., et al. 2005, A&A, 433, 807
Mannucci, F., Maiolino, R., Cresci, G., et al. 2003, A&A, 401, 519
Mäntynen, I., Kankare, E., Mattila, S., et al. 2025, A&A, 700, A199
Maoz, D., Mannucci, F., & Nelemans, G. 2014, ARA&A, 52, 107
Martí-Vidal, I., Marcaide, J. M., Alberdi, A., et al. 2007, A&A, 470, 1071
Mattila, S., & Meikle, W. P. S. 2001, MNRAS, 324, 325
Mattila, S., Väisänen, P., Farrah, D., et al. 2007, ApJL, 659, L9
McKinney, W. 2010, in Proc. 9th Python in Science Conf., ed. S. van der Walt & J. Millman (SciPy), 56
McMullin, J. P., Waters, B., Schiebel, D., Young, W., & Golap, K. 2007, ASPC, 376, 127
McQuinn, K. B. W., Skillman, E. D., Dalcanton, J. J., et al. 2012, ApJ, 759, 77
Melinder, J., Dahlen, T., Mencía Trinchant, L., et al. 2012, A&A, 545, A96
Melo, A., Ca,nameras, R., Schuldt, S., et al. 2025, A&A, 698, A264
Mengel, S., Lehnert, M. D., Thatte, N., & Genzel, R. 2002, A&A, 383, 137
Meurer, G. R., Heckman, T. M., & Calzetti, D. 1999, ApJ, 521, 64
Miettinen, O., Delvecchio, I., Smolčić, V., et al. 2017, A&A, 606, A17
Miley, G., & De Breuck, C. 2008, A&ARv, 15, 67
Miller, T. B., Chapman, S. C., Aravena, M., et al. 2018, Natur, 556, 469
Miller, T. B., Hayward, C. C., Chapman, S. C., & Behroozi, P. S. 2015, MNRAS, 452, 878
Miluzio, M., Cappellaro, E., Botticella, M. T., et al. 2013, A&A, 554, A127
Mitsuhashi, I., Tadaki, K.-i., Ikeda, R., et al. 2024, A&A, 690, A197
Mork, S. D., Gladders, M. D., Khullar, G., et al. 2025, ApJ, 979, 184
Mörtsell, E., Goobar, A., Johansson, J., & Dhawan, S. 2022a, ApJ, 933, 212
Mörtsell, E., Goobar, A., Johansson, J., & Dhawan, S. 2022b, ApJ, 935, 58
Muñoz, J. A., Kochanek, C. S., Fohlmeister, J., et al. 2022, ApJ, 937, 34
Myers, A. D., White, M., & Ball, N. M. 2009, MNRAS, 399, 2279
Napier, K., Sharon, K., Dahle, H., et al. 2023, ApJ, 959, 134
Narayan, R., & Bartelmann, M. 1996, arXiv:astro-ph/9606001
Narayanan, D., Davé, R., Johnson, B. D., et al. 2018, MNRAS, 474, 1718
Negrello, M., Amber, S., Amvrosiadis, A., et al. 2017, MNRAS, 465, 3558
Negrello, M., Hopwood, R., De Zotti, G., et al. 2010, Sci, 330, 800
Negrello, M., Hopwood, R., Dye, S., et al. 2014, MNRAS, 440, 1999
Newman, A. B., Belli, S., Ellis, R. S., & Patel, S. G. 2018, ApJ, 862, 125
Oguri, M. 2007, ApJ, 660, 1
Oguri, M., & Marshall, P. J. 2010, MNRAS, 405, 2579
Olivares, V., Treister, E., Privon, G. C., et al. 2016, ApJ, 827, 57
Osterbrock, D. E., & Ferland, G. J. 2006, Astrophysics of Gaseous Nebulae and Active Galactic Nuclei (Univ. Science Books)
Oteo, I., Ivison, R. J., Dunne, L., et al. 2018, ApJ, 856, 72
Overzier, R. A. 2016, A&ARv, 24, 14
Palicio, P. A., Matteucci, F., Della Valle, M., & Spitoni, E. 2024, A&A, 689, A203
Parra, R., Conway, J. E., Diamond, P. J., et al. 2007, ApJ, 659, 314
Pascale, M., Dai, L., McKee, C. F., & Tsang, B. T. H. 2023, ApJ, 957, 77
Pascale, M., Frye, B. L., Dai, L., et al. 2022, ApJ, 932, 85
Pascale, M., Frye, B. L., Pierel, J. D. R., et al. 2025, ApJ, 979, 13
Pavesi, R., Riechers, D. A., Sharon, C. E., et al. 2018, ApJ, 861, 43
Pérez-Torres, M., Mattila, S., Alonso-Herrero, A., Aalto, S., & Efstathiou, A. 2021, A&ARv, 29, 2
Pérez-Torres, M. A., Romero-Cañizales, C., Alberdi, A., & Polatidis, A. 2009, A&A, 507, L17
Perrotta, F., Baccigalupi, C., Bartelmann, M., De Zotti, G., & Granato, G. L. 2002, MNRAS, 329, 445
Pesce, D. W., Braatz, J. A., Reid, M. J., et al. 2020, ApJL, 891, L1
Petrushevska, T. 2020, Symm, 12, 1966
Petrushevska, T., Amanullah, R., Goobar, A., et al. 2016, A&A, 594, A54
Petrushevska, T., Goobar, A., Lagattuta, D. J., et al. 2018b, A&A, 614, A103
Petrushevska, T., Okamura, T., Kawamata, R., et al. 2018a, ARep, 62, 917
Pierel, J. D. R., Arendse, N., Ertl, S., et al. 2023, ApJ, 948, 115
Pierel, J. D. R., Frye, B. L., Pascale, M., et al. 2024a, ApJ, 967, 50
Pierel, J. D. R., Newman, A. B., Dhawan, S., et al. 2024b, ApJL, 967, L37
Pierel, J. D. R., & Rodney, S. 2019, ApJ, 876, 107
Pierel, J. D. R., Hayes, E. E., Millon, M., et al. 2026, ApJ, 998, 219
Pierel, J. D. R., Rodney, S., Vernardos, G., et al. 2021, ApJ, 908, 190
Planck Collaboration, Aghanim, N., Akrami, Y., et al. 2020, A&A, 641, A6
Planck Collaboration, Aghanim, N., Altieri, B., et al. 2015, A&A, 582, A30
Polletta, M., Frye, B. L., Garuda, N., et al. 2024, A&A, 690, A285
Polletta, M., Nonino, M., Frye, B., et al. 2023, A&A, 675, L4
Pontoppidan, K. M., Pickering, T. E., Laidler, V. G., et al. 2016, SPIE, 9910, 991016
Price, S. H., Kriek, M., Brammer, G. B., et al. 2014, ApJ, 788, 86
Puglisi, A., Daddi, E., Renzini, A., et al. 2017, ApJL, 838, L18
Puglisi, A., Rodighiero, G., Franceschini, A., et al. 2016, A&A, 586, A83
Quimby, R. M., Oguri, M., More, A., et al. 2014, Sci, 344, 396
Quimby, R. M., Werner, M. C., Oguri, M., et al. 2013, ApJL, 768, L20
Reddy, N. A., Kriek, M., Shapley, A. E., et al. 2015, ApJ, 806, 259
Refsdal, S. 1964, MNRAS, 128, 307
Reid, M. J., Braatz, J. A., Condon, J. J., et al. 2009, ApJ, 695, 287

Reid, M. J., Braatz, J. A., Condon, J. J., et al. 2013, ApJ, 767, 154
Remolina González, J. D., Sharon, K., Reed, B., et al. 2020, ApJ, 902, 44
Riechers, D. A., Capak, P. L., Carilli, C. L., et al. 2010, ApJL, 720, L131
Riess, A. G., Yuan, W., Macri, L. M., et al. 2022, ApJL, 934, L7
Robertson, A., Smith, G. P., Massey, R., et al. 2020, MNRAS, 495, 3727
Robertson, C., Holwerda, B. W., Young, J., et al. 2024, AJ, 167, 263
Robitaille, T. 2019, APLpy v2.0: The Astronomical Plotting Library in Python, v2.0, Zenodo, doi:10.5281/zenodo.2567476
Robitaille, T., & Bressert, E. 2012, APLpy: Astronomical Plotting Library in Python,, Astrophysics Source Code Library, ascl:1208.017
Rodighiero, G., Daddi, E., Baronchelli, I., et al. 2011, ApJL, 739, L40
Rodney, S. A., Brammer, G. B., Pierel, J. D. R., et al. 2021, NatAs, 5, 1118
Rodney, S. A., Strolger, L. G., Kelly, P. L., et al. 2016, ApJ, 820, 50
Roy, N., Heckman, T., Henry, A., et al. 2025, ApJ, 992, 91
Ruiter, A. J., & Seitenzahl, I. R. 2025, A&ARv, 33, 1
Rujopakarn, W., Rieke, G. H., Eisenstein, D. J., & Juneau, S. 2011, ApJ, 726, 93
Ryczanowski, D., Smith, G. P., Bianconi, M., et al. 2023, MNRAS, 520, 2547
Safarzadeh, M., Hayward, C. C., & Ferguson, H. C. 2017, ApJ, 840, 15
Sagués Carracedo, A., Goobar, A., Mörtsell, E., et al. 2024, arXiv:2406.00052
Sainz de Murieta, A., Collett, T. E., Magee, M. R., et al. 2023, MNRAS, 526, 4296
Sainz de Murieta, A., Collett, T. E., Magee, M. R., et al. 2024, MNRAS, 535, 2523
Sakamoto, K., Aalto, S., Costagliola, F., et al. 2013, ApJ, 764, 42
Salpeter, E. E. 1955, ApJ, 121, 161
Scannapieco, E., & Bildsten, L. 2005, ApJL, 629, L85
Schechter, P. L., Udalski, A., Szymański, M., et al. 2003, ApJ, 584, 657
Schmidt, M. 1959, ApJ, 129, 243
Schneider, P. 1985, A&A, 143, 413
Schneider, P., Ehlers, J., & Falco, E. E. 1992, Gravitational Lenses, Vol. 112 (Springer)
Schneider, P., Kochanek, C. S., & Wambsganss, J. 2006, Gravitational Lensing: Strong, Weak and Micro, Saas-Fee Advanced Courses 33 (Springer)
Schneider, P., & Sluse, D. 2013, A&A, 559, A37
Sedgwick, C., Serjeant, S., & Weiner, C. 2025, MNRAS, 539, 1077
Shajib, A. J., Mozumdar, P., Chen, G. C.-F., et al. 2023, A&A, 673, A9
Shapiro, I. I. 1964, PhRvL, 13, 789
Shim, H., Lee, D., Kim, Y., et al. 2022, MNRAS, 514, 2915
Shu, Y., Bolton, A. S., Mao, S., et al. 2018, ApJ, 864, 91
Shu, Y., Bolton, A. S., Mao, S., et al. 2021, ApJ, 919, 67
Simpson, J. M., Smail, I., Swinbank, A. M., et al. 2017, ApJ, 839, 58
Smartt, S. J. 2009, ARA&A, 47, 63
Smith, L. J., & Gallagher, J. S. 2001, MNRAS, 326, 1027
Smith, M., Nichol, R. C., Dilday, B., et al. 2012, ApJ, 755, 61
Smolčić, V., Miettinen, O., Tomičić, N., et al. 2017, A&A, 597, A4
Speagle, J. S., Steinhardt, C. L., Capak, P. L., & Silverman, J. D. 2014, ApJS, 214, 15
Stach, S. M., Smail, I., Amvrosiadis, A., et al. 2021, MNRAS, 504, 172
Stanishev, V., Goobar, A., Paech, K., et al. 2009, A&A, 507, 61
Strolger, L.-G., Dahlen, T., Rodney, S. A., et al. 2015, ApJ, 813, 93
Sullivan, M., Le Borgne, D., Pritchet, C. J., et al. 2006, ApJ, 648, 868
Suyu, S. H., Acebron, A., Grillo, C., et al. 2025, arXiv:2509.12319
Suyu, S. H., Goobar, A., Collett, T., More, A., & Vernardos, G. 2024, SSRv, 220, 13
Suyu, S. H., Huber, S., Ca,nameras, R., et al. 2020, A&A, 644, A162
Swinbank, A. M., Smail, I., Chapman, S. C., et al. 2004, ApJ, 617, 64
Tacconi, L. J., Genzel, R., Saintonge, A., et al. 2018, ApJ, 853, 179
Tadaki, K., Iono, D., Yun, M. S., et al. 2018, Natur, 560, 613
Takata, T., Sekiguchi, K., Smail, I., et al. 2006, ApJ, 651, 713
TDCOSMO Collaboration, Birrer, S., Buckley-Geer, E. J., et al. 2025, A&A, 704, A63
The pandas Development Team 2024, pandas-dev/pandas: pandas, v3.0.1, Zenodo, doi:10.5281/zenodo.3509134
Timmons, N., Cooray, A., Nayyeri, H., et al. 2015, ApJ, 805, 140
Treu, T. 2010, ARA&A, 48, 87
Treu, T., & Marshall, P. J. 2016, A&ARv, 24, 11
Treu, T., Suyu, S. H., & Marshall, P. J. 2022, A&ARv, 30, 8
Trombetti, T., Burigana, C., Bonato, M., et al. 2021, A&A, 653, A151
Tsujimoto, T., Yoshii, Y., Nomoto, K., et al. 1997, ApJ, 483, 228
Turner, E. L., Ostriker, J. P., & Gott, J. R., III 1984, ApJ, 284, 1
Umehata, H., Tamura, Y., Kohno, K., et al. 2015, ApJL, 815, L8
Urquhart, S. A., Bendo, G. J., Serjeant, S., et al. 2022, MNRAS, 511, 3017
Väisänen, P., Mattila, S., Kniazev, A., et al. 2008, MNRAS, 384, 886
Varenius, E., Conway, J. E., Batejat, F., et al. 2019, A&A, 623, A173
Venemans, B. P., Röttgering, H. J. A., Miley, G. K., et al. 2007, A&A, 461, 823
Verde, L., Schöneberg, N., & Gil-Marín, H. 2024, ARA&A, 62, 287
Vernardos, G., Sluse, D., Pooley, D., et al. 2024, SSRv, 220, 14
Wambsganss, J., & Paczynski, B. 1994, AJ, 108, 1156
Wang, Q. D., Diaz, C. G., Kamieneski, P. S., et al. 2024, MNRAS, 527, 10584
Wang, T.-M., Magnelli, B., Schinnerer, E., et al. 2022, A&A, 660, A142
Wardlow, J. L., Cooray, A., De Bernardis, F., et al. 2013, ApJ, 762, 59
Watkins, E. J., Barnes, A. T., Henny, K., et al. 2023, ApJL, 944, L24
Weiss, A., De Breuck, C., Marrone, D. P., et al. 2013, ApJ, 767, 88
Whitaker, K. E., Franx, M., Leja, J., et al. 2014, ApJ, 795, 104
Whitaker, K. E., Pope, A., Cybulski, R., et al. 2017, ApJ, 850, 208
Whitaker, K. E., van Dokkum, P. G., Brammer, G., & Franx, M. 2012, ApJL, 754, L29
Whitmore, B. C., Chandar, R., Schweizer, F., et al. 2010, AJ, 140, 75
Wild, V., Charlot, S., Brinchmann, J., et al. 2011, MNRAS, 417, 1760
Windhorst, R. A., Cohen, S. H., Jansen, R. A., et al. 2023, AJ, 165, 13
Witt, H. J., Mao, S., & Keeton, C. R. 2000, ApJ, 544, 98
Witt, H. J., Mao, S., & Schechter, P. L. 1995, ApJ, 443, 18
Wojtak, R., Hjorth, J., & Gall, C. 2019, MNRAS, 487, 3342
Wong, K. C., Suyu, S. H., Chen, G. C. F., et al. 2020, MNRAS, 498, 1420
Wright, E. L. 2006, PASP, 118, 1711
Yan, H., Ma, Z., Beacom, J. F., & Runge, J. 2018, ApJ, 867, 21
Young, D. R., Smartt, S. J., Mattila, S., et al. 2008, A&A, 489, 359
Zwicky, F. 1938, ApJ, 88, 529